Superconductivity and quantized anomalous Hall in rhombohedral graphene

Youngjoon Choi,[1, *] Ysun Choi,[1, *] Marco Valentini,[1, *] Caitlin L. Patterson,[1] Ludwig F. W. Holleis,[1] Owen I. Sheekey,[1] Hari Stoyanov,[1] Xiang Cheng,[1] Takashi Taniguchi,[2] Kenji Watanabe,[3] and Andrea F. Young[1, †]

[1]*Department of Physics, University of California at Santa Barbara, Santa Barbara, California 93106, USA*
[2]*Research Center for Materials Nanoarchitectonics, National Institute for Materials Science, 1-1 Namiki, Tsukuba 305-0044, Japan*
[3]*Research Center for Electronic and Optical Materials, National Institute for Materials Science, 1-1 Namiki, Tsukuba 305-0044, Japan*

(Dated: April 16, 2025)

Inducing superconducting correlations in chiral edge states is predicted to generate topologically protected zero energy modes with exotic quantum statistics [1–6]. Experimental efforts to date have focused on engineering interfaces between superconducting materials–typically amorphous metals—and semiconducting quantum Hall [7–11] or quantum anomalous Hall (QAH) [12, 13] systems. However, the strong interfacial disorder inherent in this approach can prevent the formation of isolated topological modes [14–17]. An appealing alternative is to use low-density flat band materials where the ground state can be tuned between intrinsic superconducting and quantum anomalous Hall states using only the electric field effect. However, quantized transport and superconductivity have not been simultaneously achieved. Here, we show that rhombohedral tetralayer graphene aligned to a hexagonal boron nitride substrate hosts a quantized anomalous Hall state at superlattice filling $\nu = -1$ as well as a superconducting state at $\nu \approx -3.5$ at zero magnetic field. Remarkably, gate voltage can also be used to actuate nonvolatile switching of the chirality in the quantum anomalous Hall state [18], allowing, in principle, arbitrarily reconfigurable networks of topological edge modes in locally gated devices. Thermodynamic compressibility measurements further reveal a topologically ordered fractional Chern insulator at $\nu = 2/3$ [19]—also stable at zero magnetic field—enabling proximity coupling between superconductivity and fractionally charged edge modes. Finally, we show that, as in rhombohedral bi- and trilayers [20–22], integrating a transition metal dichalcogenide layer to the heterostructure nucleates a new superconducting pocket [20–24], while leaving the topology of the $\nu = -1$ quantum anomalous Hall state intact. Our results pave the way for a new generation of hybrid interfaces between superconductors and topological edge states in the low-disorder limit.

INTRODUCTION

The discovery of superconductivity in 1911 and the quantized Hall effect [25] in 1980 together have come to define the two dominant paradigms–based on symmetry breaking and on topology, respectively—for understanding condensed matter systems. In recent years, there has been intense interest in the possibility of introducing superconducting pairing to the chiral edge modes of the quantum Hall state, as this combination is predicted to give rise to new modes with unconventional quantum statistics [1, 2, 4–6], and allow for the creation of electronic devices with novel functionality [3]. Practically, however, interfacing superconductivity with chiral edge modes is rendered challenging by the incompatibility of materials hosting these paradigmatic zero-resistance states: superconductivity is most common in high density metals, while quantized Hall effects typically occur in low carrier density semiconducting materials. As a result, interpretation of experimental data has had to contend with the effects of disorder arising from the interface between different materials. Two dimensional flat band systems such as twisted bilayer graphene, transition metal dichalcogenide homo- and heterobilayers, and rhombohedral graphene multilayers provide the opportunity to circumvent this challenge. In all of these systems, a high density of states provides the setting for intrinsic superconductivity and magnetism, while the Berry curvature native to honeycomb materials generically leads to topological bands. However, to date no single device has shown both quantized anomalous Hall transport and intrinsic superconductivity at zero magnetic field. In twisted bilayer graphene, gate tunability between a superconductor and magnetic state was demonstrated, but without quantized edge state transport [26]. In twisted WSe₂, thermodynamic signatures of quantum anomalous Hall states were observed [27], but in a different regime of twist angle than superconductivity [28, 29]. Other TMD systems such as twisted MoTe₂ and MoTe₂/WSe₂ show integer and fractionally quantized edge transport [30, 31], but no superconductivity has been reported.

Rhombohedral graphene multilayers provide an appealing alternative due to their low disorder and high experimental reproducibility. Absent crystallographic alignment to an hBN cladding layer, superconductivity and magnetic metallic states have been observed in both bi- and trilayer systems [20–22, 24, 32–34]. Integrating a moiré potential via hBN alignment allows for quantized anomalous Hall states at finite carrier density via commensuration with the moiré superlattice potential. Signatures of a QAH state were first observed in aligned trilayers [35], albeit without quantization at zero magnetic field. Signatures of superconductivity were also reported in this system [36]; however, the resistance of this state saturated to several hundred ohms at low temperature, and was resilient to perpendicular magnetic fields as large as 1T—features which subsequent work has shown to be uncharacteristic of rhombohedral graphene superconduc-
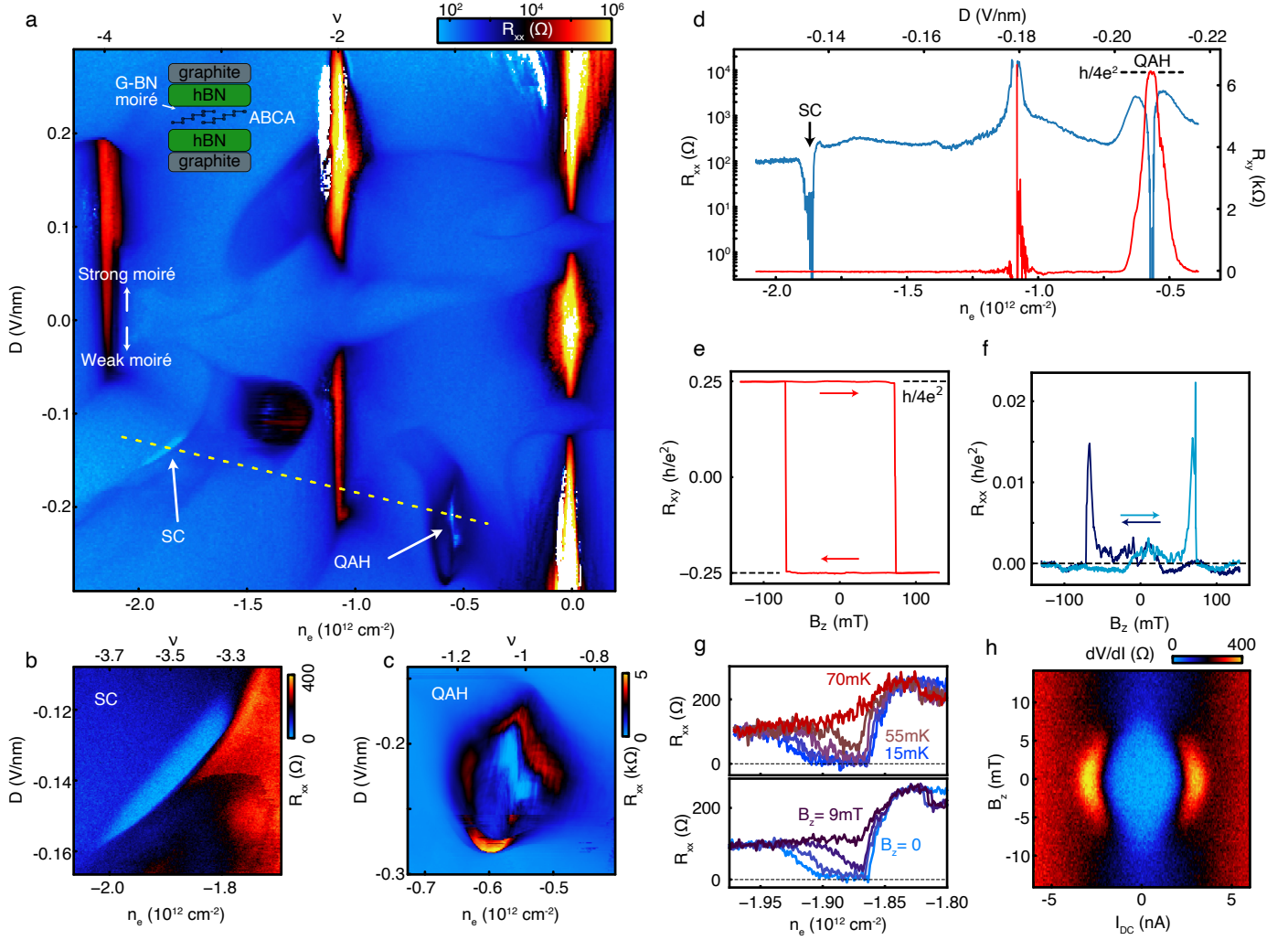
FIG. 1. **Gate-tunable superconductivity and quantized anomalous Hall effect in hBN aligned rhombohedral tetralayer graphene. a**, R_{xx} as a function of n_e and D. Zero resistance superconductivity (SC) and quantized anomalous Hall (QAH) states are indicated. Inset: device schematic, showing rhombohedral tetralayer with ABCA stacking order, encapsulating hexagonal boron nitride (hBN) layers and graphite gates. The crystal axes of the top hBN and graphene tetralayer are aligned, so that hole carriers occupy the layer with strong moiré potential for $D > 0$, as indicated (See Methods and Fig. ED1 for the device details). **b, c**, Detail of R_{xx} around the the superconducting pocket (**b**) and the QAH region at $\nu = -1$ (**c**). **d**, R_{xx} and R_{xy}, measured along the trajectory indicated in panel **a**. **e, f**, R_{xy} and R_{xx} within the $\nu = -1$ quantum anomalous Hall plateau measured as a function of B_z at $n_e = -0.564 \times 10^{12}\,\mathrm{cm}^{-2}$, $D = -0.208\,\mathrm{V/nm}$. **g**, T and B_z dependence of R_{xx} in the superconducting pocket at $D = -0.138\,\mathrm{V/nm}$. **h**, Nonlinear resistivity measured as a function of B_z and I_{DC} in the superconducting pocket at $n_e = -1.879 \times 10^{12}\,\mathrm{cm}^{-2}$, $D = -0.138\,\mathrm{V/nm}$.

tors [20–23, 33, 34]. More recently, both integer and fractional QAH states were reported in aligned pentalayers [19] and hexalayers [37]. These results motivate the search for superconductivity in aligned rhombohedral multilayers.

SUPERCONDUCTIVITY AND QAH EFFECT

Here, we report the observation of superconductivity and quantized anomalous Hall effect in hBN aligned rhombohedral tetralayer graphene. Fig. 1a shows the carrier density-(n_e) and displacement field (D) dependent longitudinal resis-

tance (R_{xx}) of Device A, measured for magnetic field $B = 0$ and temperature $T = 15\,\mathrm{mK}$. High resistance features are observed at $|n_e| = (2.15 \pm 0.05) \times 10^{12}\,\mathrm{cm}^{-2}$, which we associate with full filling ($\nu = \pm 4$) of the moiré unit cell [38] giving an estimated moiré lattice constant of $\lambda = 14.5-14.8\,\mathrm{nm}$. Here we focus on two distinct pockets where $R_{xx} = 0$ observed for $D < 0$ where the carriers are polarized away from the aligned hBN interface (see Fig. 1b-c). Fig. 1d shows R_{xx} and R_{xy} measured along the trajectory indicated in Fig. 1a. R_{xx} drops below $10\,\Omega$ within each pocket; the two states show contrasting R_{xy}, which vanishes for the high hole-density pocket near $n_e \approx -1.9 \times 10^{12}\,\mathrm{cm}^{-2}$ (consistent with a su-

perconducting state) but is quantized to $R_{xy} = h/4e^2$ at $n_e \approx -0.6 \times 10^{12}\,\mathrm{cm}^{-2}$, corresponding to $\nu = -1$ moiré filling. B_z dependent measurements within this state indeed show hysteretic switching between quantized values of $\pm h/4e^2$ (Fig. 1e), concomitant with $R_{xx} < .01h/e^2$ (Fig. 1f), consistent with a quantized anomalous Hall state with Chern number $|C| = 4$ as theoretically predicted [39, 40]. Temperature dependent measurements at this filling show behavior consistent with a magnetic Curie temperature of $4.5\,\mathrm{K}$ and a thermal activation gap of $\Delta \approx 10\,\mathrm{K}$ (see Fig. ED3).

To confirm the identification of the superconducting phase, we study the temperature, current, and perpendicular magnetic field dependence of the zero-resistance state in Figs. 1g-h. Superconductivity is suppressed for temperatures $T > T_C \approx 55\,\mathrm{mK}$ and perpendicular magnetic field $B_z > B_c \approx 7\,\mathrm{mT}$, and shows a critical current of $I_C \approx 2\,\mathrm{nA}$. These observations are in-line with existing work on unaligned rhombohedral trilayers [33] and Bernal bilayers [34] encapsulated in hexagonal boron nitride. Further evidence for superconductivity in the high-density pocket is a flux-tuned oscillation in the critical current observed for certain dopings, confirming the macroscopic phase coherence of the superconducting state (see Fig. ED4). Notably, the domain of superconductivity is reminiscent of hole-doped rhombohedral trilayer graphene, where superconductivity arises in a narrow strip bounded at lower $|n_e|$ by a sharp phase boundary likely associated with isospin symmetry breaking [33]. An additional superconducting state is also observed near $\nu = -2$ on the strong moiré side, with a critical temperature $T_c \approx 90$ mK, described in Extended Data Fig. ED5).

CONTROLLABLE SWITCHING OF QAH EDGE CHIRALITY

Figs. 2a-b show R_{xy} measured in the vicinity of the $\nu = -1$ quantum anomalous Hall state at a nominal applied magnetic field $B_z \approx 0$ and $B_\parallel = 10$ mT. For these measurements, D is the fast axis, with n_e stepped between traces from left to right. Figs. 2a and 2b differ only in the direction of the D-axis sweep. Both show quantized transport, but with opposite signs of quantized R_{xy} at the same n_e and D values, implying an electric field induced reversal of the valley polarization. The switching effect is nonvolatile. As shown in Fig. 2c, the chirality can be controllably reversed by excursions in the applied D, with the value of R_{xy} remaining stable between excursions when D is returned to the same value.

Electric field control of magnetic switching has been reported previously in twisted and rhombohedral graphene multilayers [18, 41–44]. Switching can also arise in metallic states due purely to the density-dependent orbital magnetization of Bloch states with finite Berry curvature, as occurs in the current sample near $\nu = -2.5$ (see Fig. ED6). The key microscopic requirement is that the magnetization changes sign within a phase with fixed valley polarization [45]. Time reversal symmetry mandates that the magnetic moment of states in

opposite valleys have opposite signs ($m_{K'} = -m_K$), and at zero magnetic field, the valley polarization in an orbital magnet is chosen spontaneously. Indeed, entering a valley polarized phase at $B_z = 0$ often results in switchy behavior associated with the randomly chosen valley polarization, visible in Figs. 1a, c, and ED7a. At small but finite B_z, the valley degeneracy is lifted, introducing a valley splitting $\Delta E = 2m_K B_z$ between the two valleys. Electrons polarized within the K valley will only be in the ground state for $m_K > 0$; if m_K becomes negative, a K-polarized state will become metastable, and may persist in the presence of an energy barrier separating K and K' polarizations.

Notably, in the present system switching is effective only when the D range is sufficiently large to exit and reenter the valley polarized phase, with no relaxation observed for parameter sweeps *within* the valley polarized phase at low B_z. This behavior can be explained if, upon entry to the valley polarized phase, the system polarizes in the low energy valley, but the low energy valley switches from K to K' within the valley polarized phase. Fig. 2d shows a schematic energy level diagram along with the trajectory of the system for rising and falling D. A finite energy barrier prevents relaxation throughout the valley polarized phase, resulting in the stable switching observed. Interestingly, reliable nonvolatile switching does not occur for $B_\parallel = 0$ (see Fig. ED8), suggesting that $B_\parallel$ suppresses partially valley polarized phases along the gate tuned trajectory in which relaxation barriers are small.

As expected for magnetic systems, bistable behavior is eventually destroyed by sufficiently large B_z. Figs. 2e-f show R_{xy} measured as a function of D and B_z. Above a threshold value of B_z, the bistable regime shrinks and eventually vanishes at $B_z \approx 50$ mT. Fig. 2g describes a mechanism for this suppression. In the absence of thermal relaxation, the system remains in a metastable valley as long as the barrier is finite. Applied magnetic field destroys the barrier when ΔE becomes comparable to the barrier height E^*, allowing the system to relax to the ground state.

FRACTIONAL CHERN INSULATOR AT ZERO FIELD

Signatures of topologically nontrivial gapped phases are also evident in measurements of the inverse compressibility, $\kappa = \partial\mu/\partial n_e$, shown in Fig. 3a. Numerous peaks in the inverse compressibility corresponding to correlated insulator states are observed at both integer ($\nu = -2, -1, 1, 2$) and fractional ($\nu = \frac{1}{3}, \frac{2}{3}$) moiré filling; for example, the incompressible peak corresponding to the $C = -4$ state at $\nu = -1$ is shown inset to Fig. 3a. To determine the Chern number of these states, we measure the B_z-dependence of the density, n_e at which the incompressible peak appears. For a gapped state, the density changes according to the Streda formula[46].

Fig. 3b shows this measurement at $\nu = -1$; as expected from the measured quantized Hall conductance, the incompressible peak disperses linearly with a slope consistent with $C = -4$. Applying this to other correlated insulators, we find
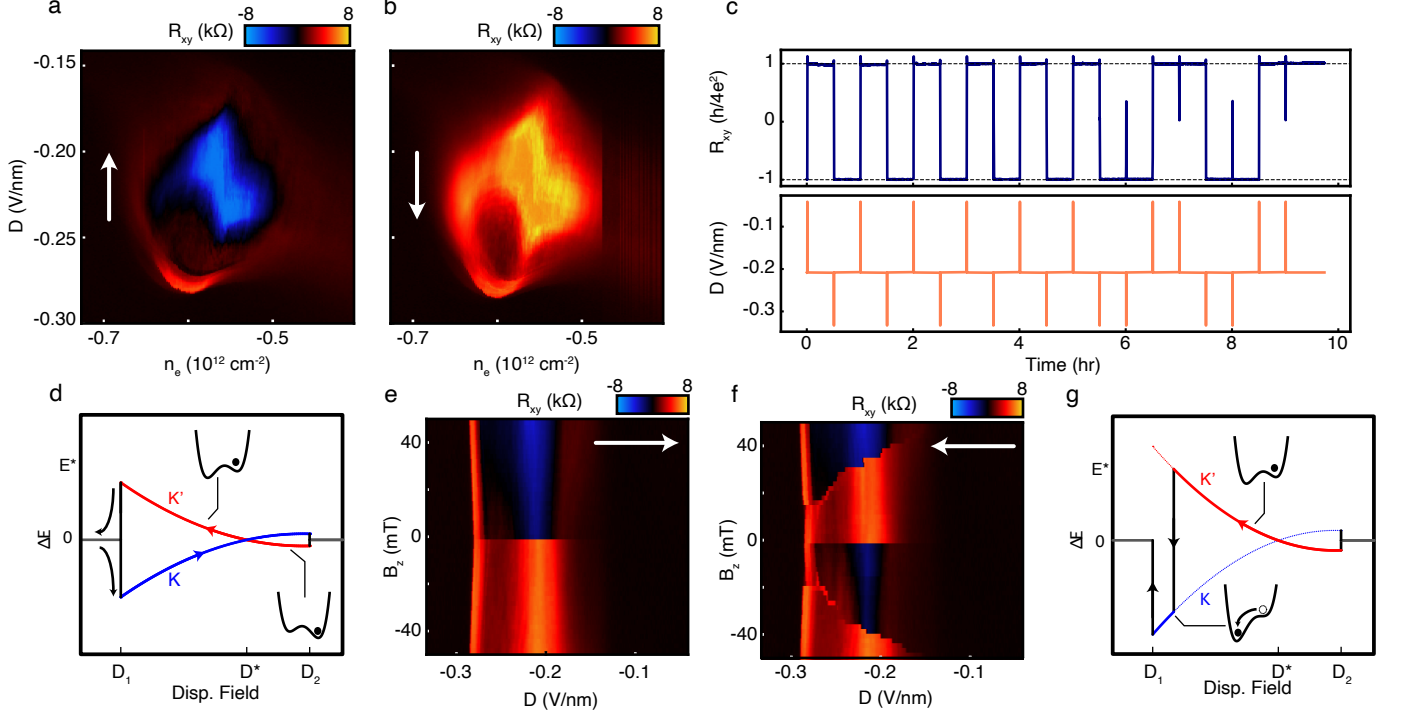
FIG. 2. **Electric switching of edge mode chirality. a**, R_{xy} measured as a function of n_e and D with $B_\parallel = 10\,\mathrm{mT}$ near $\nu = -1$. D is swept from low to high, and n_e incremented between sweeps. **b**, The same as panel **a**, with D swept high to low. **c**, Time dependence of R_{xy} (top panel) during a series of rapid excursion in D (bottom panel). **d**, Schematic diagram of $\Delta E = -Bm_{K(K')}$ at low B_z. Along the D-tuned trajectory, the system goes from valley unpolarized to a valley polarized phase at D_1; within the valley polarized phase, $m_K = -m_{K'}$ changes sign at D^*; and the system undergoes a second transition to a valley unpolarized phase at $D = D_2$. Upon entry to the polarized phase, the system polarizes into the low energy valley, but due to the finite energy barrier the system remains trapped in this valley even after it no longer corresponds to the ground state. This results in opposite valley polarization throughout the valley polarized phase for opposite sweep directions. Insets show schematics of the free energy as a function of valley polarization n_k. **e**, R_{xy} as a function of D and B_z with fixed $B_\parallel = 10\,\mathrm{mT}$. D is swept low to high. **f**, The same as panel **e**, with D swept high to low. **g**, Energy level schematic at higher applied B_z. The system relaxes at $\Delta E = E^*$, where the barrier vanishes.

the $\nu = 1$ state for $D > 0$ (i.e., the layer polarization corresponding to a weak moiré potential) is a Chern insulator with $C = 1$ persisting to $B = 0$. The adjacent $\nu = 2/3$ state shows $C = 2/3$, making it a fractional Chern insulator [19, 31, 37]. As summarized in Fig. 3d, most of the other observed incompressible phases have zero Chern number, including those at $\nu = \frac{1}{3}$ and $\frac{2}{3}$ for $D < 0$ (corresponding to the regime of strong moiré potential).

Our compressibility measurements allow us to quantitatively determine the thermodynamic gaps of the Chern insulator state via the relation $\Delta\mu = \int(\kappa)\mathrm{d}n_e$; the gap is equivalent to the area of the compressibility peaks shown in Fig. 3e. In a clean system, this gap corresponds to the energy difference between adding and subtracting a single electron from the incompressible ground state. Fig. 3f shows the temperature dependence of the thermodynamic gap Δ for the topologically nontrivial states at $\nu = \pm 1$ and $\frac{2}{3}$. The fractional Chern insulator shows a gap of $\Delta \approx 2.7\,\mathrm{K}$ at the lowest temperatures.

SPIN-ORBIT INDUCED SUPERCONDUCTIVITY

Prior work on Bernal bilayer [20, 23, 24] and rhombohedral trilayer [21, 22] graphene have shown that the domain and critical temperature of superconductivity are significantly enhanced by incorporating a transition metal dichalcogenide cladding layer. Notably, in these devices, spin-orbit enhanced superconductivity is observed when carriers are polarized to the graphene layer *closest* to the dichalcogenide substrate [47–49]. In hBN aligned rhombohedral multilayers [19, 35], Chern insulators are observed when carriers are polarized *away* from the aligned hBN. Spin-orbit enhanced superconductivity and topologically nontrivial bands are thus compatible, and may be realized by replacing the misaligned hBN substrate with a dichalcogenide layer.

Fig. 4 shows R_{xx} measured in Device D, which consists of a rhombohedral tetralayer sample encapsulated between WS$_2$ and hBN flakes. The alignment of the hBN and graphene crys-
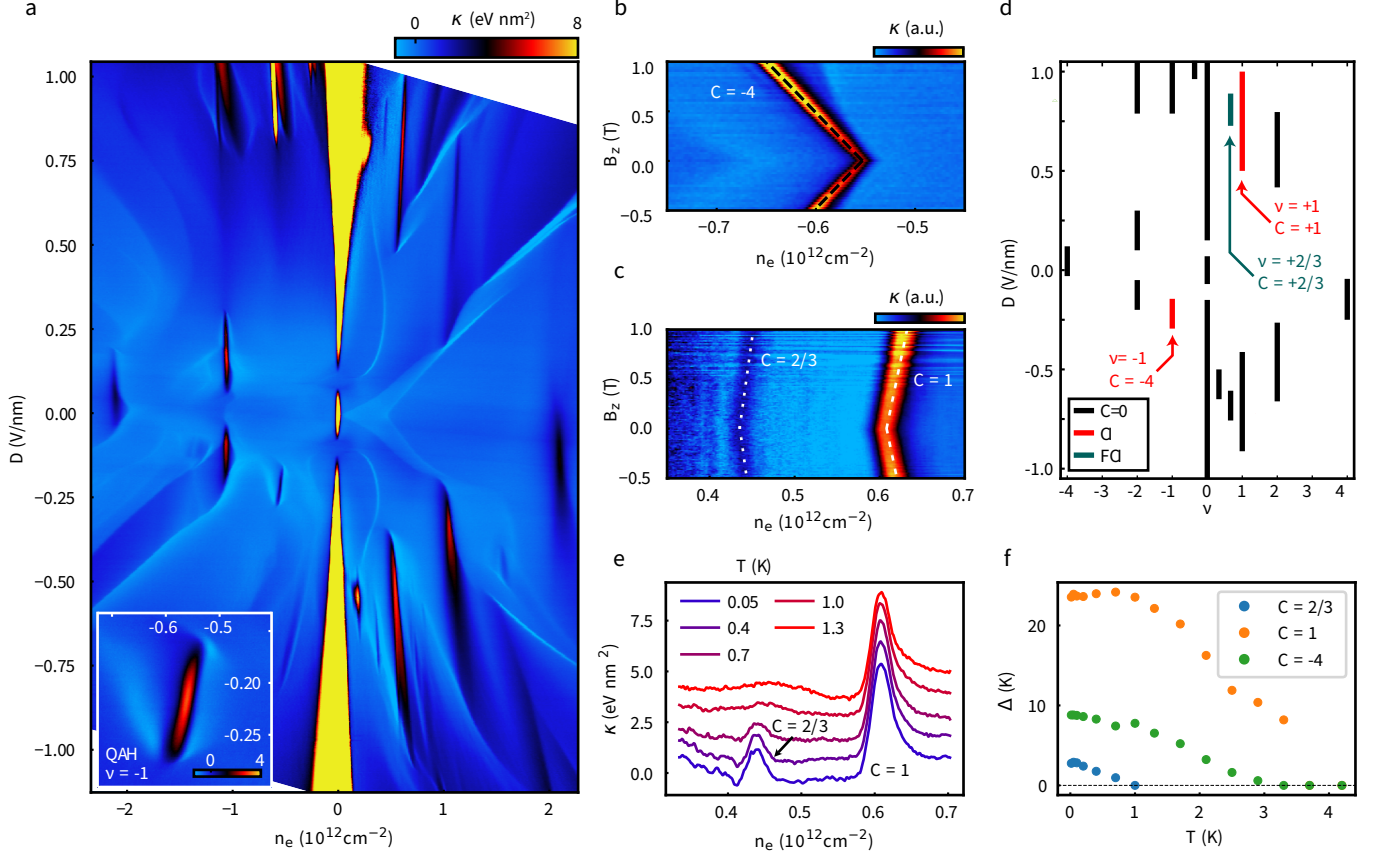
FIG. 3. **Integer and fractional Chern insulators revealed by inverse compressibility measurements. a**, n_e- and D-dependent inverse compressibility $\kappa = \partial\mu/\partial n_e$. Gapped states manifest as peaks in κ at fixed commensurate filling. Note that constant ν contours are not vertical on this scale, due to the quantum capacitance of the strong insulator at the charge neutrality. Inset: κ near the $\nu = -1$ QAH state. **b**, magnetic field dependence of κ near the $\nu = -1$ QAH state measured at $D = -0.208\,\text{V/nm}$. The Streda slope is consistent with $C = -4$. **c**, Magnetic field dependence of κ for $\nu = 1$ and $2/3$ at $D = 0.885\,\text{V/nm}$. Their slope difference is consistent with a $C = 1$ and $C = 2/3$, respectively. See Fig. ED2. **d**, Classification of correlated incompressible peaks shown in **a**. **e**, Temperature dependence of κ for $C = 2/3$ and $C = 1$ Chern insulators at $D = 0.885\,\text{V/nm}$. $C = 2/3$ state is suppressed for $T \approx 1\,\text{K}$. Curves are offset by $1\,\text{eV nm}^2$ for clarity. **f**, Thermodynamic gap extracted from κ (see Fig. ED3) as a function of temperature for $C = 2/3, 1$ and -4 Chern insulators of panels **b** and **c**.

tal lattices produces a moiré lattice with $\lambda \approx 12\,\text{nm}$, suggesting a small rotational misalignment. Here, $D \cdot n_e > 0$ corresponds to strong spin-orbit proximity effect and weak moiré potential. We observe two zero-resistance pockets in this regime for hole doping, marked SC1 and SC2. SC1 appears in a similar parameter regime to the superconductivity in the bare, hBN encapsulated tetralayer shown in Fig. 1 (see Fig. ED9). The transition temperature of SC1 is somewhat reduced in the presence of WS$_2$, showing a maximum $T_c \approx 35\,\text{mK}$ (Fig. 4b), a 30% reduction as compared to Device A. On the contrary, SC2 displays $T_c \approx 85\,\text{mK}$ (Fig.4c), which is 50% higher than the T_c of the weak-moiré SC in Device A. SC2 has no analog in the bare rhombohedral tetralayer aligned to hBN of Fig. 1a, but bears a striking resemblance in terms of n_e- and D- range to the superconduct-

ing pocket recently discovered in WSe$_2$ supported rhombohedral trilayer [21, 22], appearing near the low-$|D|$ boundary of an ordered state. Measurements of the in-plane critical field, moreover, show significant violation of the Pauli limit for SC1, but suppression of the in-plane critical field as compared to the Pauli limit for SC2 (see Fig. ED9). This is consistent with the increased role of orbital depairing at low D thought to limit in-plane critical fields in spin-orbit enhanced graphene superconductors [23].

The phase diagram of Device D is qualitatively similar to that of the hBN encapsulated samples. Although the anomalous Hall signal is not quantized at $\nu = -1$ (See Fig. ED10, a fact we attribute to sample inhomogeneity), an incompressible state with Streda slope consistent with $C = -4$ (Fig. 4d) is observed just as in Devices A, B and C. Notably, thermo-
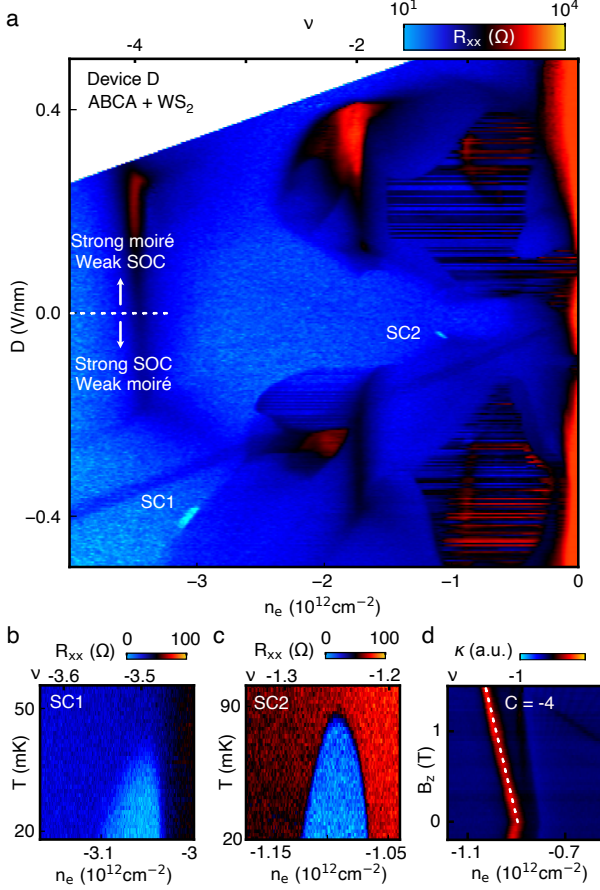
FIG. 4. **Superconductivity and Chern insulator in spin-orbit coupled rhombohedral tetralayer graphene with moiré superlattice. a**, R_{xx} as a function of D and n_e. Two regions of superconductivity are observed: SC1 at higher hole density and $|D|$, and SC2 at lower $|n_e|$ and $|D|$. **b, c**, Superconducting domes, R_{xx} as a function of T and n_e for SC1 at $D = -0.399\,\text{V/nm}$ and SC2 at $D = -0.043\,\text{V/nm}$. **d**, κ around $\nu = -1$ as a function of B_z and n_e taken at $D = -0.37\,\text{V/nm}$, showing non-trivial Chern number $C = -4$.

dynamic measurements in Device D do reveal some discrepancies with the other devices. For example, Device D shows an incompressible phase at $\nu = -1$ on the strong moiré side that is absent in Device A, B, and C. This difference may arise either from different hBN-graphene twist angle or the proximity-induced spin-orbit coupling, although we note that the anomaly appears for the weak spin-orbit coupling sign of layer polarization.

DISCUSSION

Our measurements show that rhombohedral tetralayer graphene hosts all of the ingredients required for creating low disorder interfaces between superconducting states and a va-riety of chiral edge modes. We note that these features are unlikely to be unique to tetralayer graphene, and are expected to eventually be observed across a range of layer numbers. Our work shows that integer and fractional Chern insulators at $\nu = 1$ and $\nu = 2/3$—previously reported only in 5 and 6 layer samples—occur in 4 layer rhombohedral graphene as well. At the same time, we find superconductivity—previously observed only in 2 and 3 layer systems without hBN alignment—persists to 4 layers and moreover survives a finite moiré potential. This suggests a large parameter space of substrate choice and graphene-substrate alignment angle [50] within which to optimize superconducting parameters. Even without further optimization, however, the exceptional gate tunability of rhombohedral tetralayer graphene already allows new experiments to probe the interface of superconducting and topological phases.

Author Contributions. YJC fabricated devices A-C with the help of YSC and HS. CP fabricated device D with the help of XC. YJC, YSC, and MV performed transport and capacitance experiments on devices A-C, assisted by LFWH. MV, YSC and LFWH measured device D, assisted by CLP and OIS. TT and KW provided the hexagonal boron nitride crystals. YJC, YSC, MV, and AFY analyzed the data and wrote the paper. All coauthors reviewed the manuscript prior to submission.

---

* These authors contributed equally
† andrea@physics.ucsb.edu

[1] Qi, X.-L., Hughes, T. L. & Zhang, S.-C. Chiral topological superconductor from the quantum Hall state. Physical Review B **82**, 184516 (2010). URL https://link.aps.org/doi/10.1103/PhysRevB.82.184516.

[2] Clarke, D. J., Alicea, J. & Shtengel, K. Exotic non-Abelian anyons from conventional fractional quantum Hall states. Nature Communications **4**, 1348 (2013). URL http://www.nature.com/ncomms/journal/v4/n1/abs/ncomms2340.html.

[3] Clarke, D. J., Alicea, J. & Shtengel, K. Exotic circuit elements from zero-modes in hybrid superconductor-quantum-Hall systems. Nature Physics **10**, 877–882 (2014). URL http://www.nature.com/nphys/journal/v10/n11/full/nphys3114.html.

[4] Mong, R. S. K. et al. Universal Topological Quantum Computation from a Superconductor-Abelian Quantum Hall Heterostructure. Physical Review X **4**, 011036 (2014). URL http://link.aps.org/doi/10.1103/PhysRevX.4.011036.

[5] Lian, B., Sun, X.-Q., Vaezi, A., Qi, X.-L. & Zhang, S.-C. Topological quantum computation based on chiral Majorana fermions. Proceedings of the National Academy of Sciences **115**, 10938–10942 (2018). URL https://www.pnas.org/content/115/43/10938.

[6] Lindner, N. H., Berg, E., Refael, G. & Stern, A. Fractionalizing Majorana Fermions: Non-Abelian Statistics on the Edges of Abelian Quantum Hall States. Phys. Rev. X **2** (2012). URL http://link.aps.org/doi/10.1103/PhysRevX.2.041002.

[7] Lee, G.-H. et al. Inducing superconducting correlation in quantum Hall edge states. Nature Physics **13**, 693–698 (2017). URL https://www.nature.com/articles/nphys4084.

[8] Amet, F. et al. Supercurrent in the quantum Hall regime. Science **352**, 966–969 (2016). URL http://science.sciencemag.org/content/352/6288/966.

[9] Vignaud, H. et al. Evidence for chiral supercurrent in quantum Hall Josephson junctions. Nature **624**, 545–550 (2023). URL https://www.nature.com/articles/s41586-023-06764-4. Publisher: Nature Publishing Group.

[10] Gul, O. et al. Andreev Reflection in the Fractional Quantum Hall State. Physical Review X **12**, 021057 (2022). URL https://link.aps.org/doi/10.1103/PhysRevX.12.021057.

[11] Barrier, J. et al. One-dimensional proximity superconductivity in the quantum Hall regime. Nature **628**, 741–745 (2024). URL https://www.nature.com/articles/s41586-024-07271-w.

[12] Uday, A. et al. Induced superconducting correlations in a quantum anomalous Hall insulator. Nature Physics 1–7 (2024). URL https://www.nature.com/articles/s41567-024-02574-1. Publisher: Nature Publishing Group.

[13] Atanov, O. et al. Proximity-induced quasi-one-dimensional superconducting quantum anomalous Hall state. Cell Reports Physical Science **5** (2024). URL https://www.cell.com/cell-reports-physical-science/abstract/S2666-3864(23)00607-0. Publisher: Elsevier.

[14] Tang, Y., Knapp, C. & Alicea, J. Vortex-enabled Andreev processes in quantum Hall–superconductor hybrids. Physical Review B **106**, 245411 (2022). URL https://link.aps.org/doi/10.1103/PhysRevB.106.245411.

[15] Kurilovich, V. D., Raines, Z. M. & Glazman, L. I. Disorder-enabled Andreev reflection of a quantum Hall edge. Nature Communications **14**, 2237 (2023). URL https://www.nature.com/articles/s41467-023-37794-1. Publisher: Nature Publishing Group.

[16] Kurilovich, V. D. & Glazman, L. I. Criticality in the Crossed Andreev Reflection of a Quantum Hall Edge. Physical Review X **13**, 031027 (2023). URL https://link.aps.org/doi/10.1103/PhysRevX.13.031027.

[17] Ji, W. & Wen, X.-G. ½(e²/h) Conductance Plateau without 1D Chiral Majorana Fermions. Physical Review Letters **120**, 107002 (2018). URL https://link.aps.org/doi/10.1103/PhysRevLett.120.107002.

[18] Polshyn, H. et al. Electrical switching of magnetic order in an orbital Chern insulator. Nature **588**, 66–70 (2020). URL http://www.nature.com/articles/s41586-020-2963-8.

[19] Lu, Z. et al. Fractional quantum anomalous Hall effect in multilayer graphene. Nature **626**, 759–764 (2024).

[20] Zhang, Y. et al. Enhanced superconductivity in spin–orbit proximitized bilayer graphene. Nature **613**, 268–273 (2023). URL https://www.nature.com/articles/s41586-022-05446-x.

[21] Patterson, C. L. et al. Superconductivity and spin canting in spin-orbit proximitized rhombohedral trilayer graphene (2024). URL http://arxiv.org/abs/2408.10190. ArXiv:2408.10190 [cond-mat].

[22] Yang, J. et al. Diverse Impacts of Spin-Orbit Coupling on Superconductivity in Rhombohedral Graphene (2024). URL http://arxiv.org/abs/2408.09906. ArXiv:2408.09906 [cond-mat].

[23] Holleis, L. et al. Nematicity and Orbital Depairing in Superconducting Bernal Bilayer Graphene with Strong Spin Orbit Coupling (2024). URL http://arxiv.org/abs/2303.00742. ArXiv:2303.00742.

[24] Li, C. et al. Tunable superconductivity in electron- and hole-doped Bernal bilayer graphene. Nature **631**, 300–306 (2024). URL https://www.nature.com/articles/s41586-024-07584-w.

[25] Klitzing, K. v., Dorda, G. & Pepper, M. New Method for High-Accuracy Determination of the Fine-Structure Constant Based on Quantized Hall Resistance. Phys. Rev. Lett. **45**, 494–497 (1980). URL http://link.aps.org/doi/10.1103/PhysRevLett.45.494.

[26] Stepanov, P. et al. Competing Zero-Field Chern Insulators in Superconducting Twisted Bilayer Graphene. Physical Review Letters **127**, 197701 (2021). URL https://link.aps.org/doi/10.1103/PhysRevLett.127.197701.

[27] Foutty, B. A. et al. Mapping twist-tuned multiband topology in bilayer WSe2. Science **384**, 343–347 (2024). URL https://www.science.org/doi/10.1126/science.adi4728. Publisher: American Association for the Advancement of Science.

[28] Xia, Y. et al. Unconventional superconductivity in twisted bilayer WSe2 (2024). URL http://arxiv.org/abs/2405.14784. ArXiv.2405.14784.

[29] Guo, Y. et al. Superconductivity in twisted bilayer WSe$_2$ (2024). URL http://arxiv.org/abs/2406.03418. ArXiv:2406.03418.

[30] Li, T. et al. Quantum anomalous Hall effect from intertwined moiré bands. Nature **600**, 641–646 (2021). URL https://www.nature.com/articles/s41586-021-04171-1.

[31] Park, H. et al. Observation of fractionally quantized anomalous Hall effect. Nature **622**, 74–79 (2023). URL https://www.nature.com/articles/s41586-023-06536-0.

[32] Zhou, H. et al. Half- and quarter-metals in rhombohedral trilayer graphene. Nature **598**, 429–433 (2021). URL https://www.nature.com/articles/s41586-021-03938-w.

[33] Zhou, H., Xie, T., Taniguchi, T., Watanabe, K. & Young, A. F. Superconductivity in rhombohedral trilayer graphene. Nature **598**, 434–438 (2021). URL https://www.nature.com/articles/s41586-021-03926-0.

[34] Zhou, H. et al. Isospin magnetism and spin-polarized superconductivity in Bernal bilayer graphene. Science **375**, 774–778 (2022). URL https://www.science.org/doi/10.1126/science.abm8386.

[35] Chen, G. et al. Tunable correlated Chern insulator and ferromagnetism in a moiré superlattice. Nature **579**, 56–61 (2020). URL https://www.nature.com/articles/s41586-020-2049-7.

[36] Chen, G. et al. Signatures of tunable superconductivity in a trilayer graphene moiré superlattice. Nature **572**, 215–219 (2019). URL https://www.nature.com/articles/s41586-019-1393-y.

[37] Xie, J. et al. Even- and Odd-denominator Fractional Quantum Anomalous Hall Effect in Graphene Moire Superlattices (2024). URL http://arxiv.org/abs/2405.16944. ArXiv:2405.16944 [cond-mat].

[38] Chen, G. et al. Evidence of a gate-tunable Mott insulator in a trilayer graphene moiré superlattice. Nature Physics **15**, 237 (2019). URL https://www.nature.com/articles/s41567-018-0387-2.

[39] Zhang, F., Jung, J., Fiete, G. A., Niu, Q. & MacDonald, A. H. Spontaneous quantum hall states in chirally stacked few-layer graphene systems. Physical review letters **106**, 156801 (2011).

[40] Park, Y., Kim, Y., Chittari, B. L. & Jung, J. Topological flat bands in rhombohedral tetralayer and multilayer graphene on hexagonal boron nitride moiré superlattices. Physical Review B **108**, 155406 (2023).

[41] Grover, S. et al. Chern mosaic and Berry-curvature magnetism in magic-angle graphene. Nature Physics **18**, 885–892 (2022). URL https://www.nature.com/articles/s41567-022-01635-7. Publisher: Nature Publishing Group.

[42] Han, T. et al. Orbital multiferroicity in pentalayer rhombohedral graphene. Nature **623**, 41–47 (2023). URL https://www.nature.com/articles/s41586-023-06572-w. Number: 7985 Publisher: Nature Publishing Group.

[43] Su, R. et al. Generalized anomalous Hall crystals in twisted bilayer-trilayer graphene (2024). URL http://arxiv.org/abs/2406.17766. ArXiv:2406.17766 [cond-mat].

[44] Sha, Y. et al. Observation of a Chern insulator in crystalline ABCA-tetralayer graphene with spin-orbit coupling. Science **384**, 414–419 (2024). URL https://www.science.org/doi/10.1126/science.adj8272. Publisher: American Association for the Advancement of Science.

[45] Zhu, J., Su, J.-J. & MacDonald, A. H. Voltage-Controlled Magnetic Reversal in Orbital Chern Insulators. Physical Review Letters **125**, 227702 (2020). URL https://link.aps.org/doi/10.1103/PhysRevLett.125.227702.

[46] Streda, P. Quantised Hall effect in a two-dimensional periodic potential. J. Phys. C: Solid State Phys. **15** (1982).

[47] Khoo, J. Y., Morpurgo, A. F. & Levitov, L. On-Demand Spin-Orbit Interaction from Which-Layer Tunability in Bilayer Graphene. Nano Letters **17**, 7003–7008 (2017). URL https://doi.org/10.1021/acs.nanolett.7b03604.

[48] Gmitra, M. & Fabian, J. Proximity Effects in Bilayer Graphene on Monolayer WSe2: Field-Effect Spin Valley Locking, Spin-Orbit Valve, and Spin Transistor. Physical Review Letters **119**, 146401 (2017). URL https://link.aps.org/doi/10.1103/PhysRevLett.119.146401.

[49] Island, J. O. et al. Spin–orbit-driven band inversion in bilayer graphene by the van der Waals proximity effect. Nature **571**, 85–89 (2019). URL http://www.nature.com/articles/s41586-019-1304-2.

[50] Zhang, Y. et al. Twist-Programmable Superconductivity in Spin-Orbit Coupled Bilayer Graphene (2024). URL http://arxiv.org/abs/2408.10335. ArXiv:2408.10335 [cond-mat].

[51] Li, H. et al. Electrode-Free Anodic Oxidation Nanolithography of Low-Dimensional Materials. Nano Letters **18**, 8011–8015 (2018). URL https://doi.org/10.1021/acs.nanolett.8b04166.

[52] Kim, H. et al. Imaging inter-valley coherent order in magic-angle twisted trilayer graphene. Nature 1–7 (2023). URL https://www.nature.com/articles/s41586-023-06663-8.

[53] Li, H. et al. Global Control of Stacking-Order Phase Transition by Doping and Electric Field in Few-Layer Graphene. Nano Letters **20**, 3106–3112 (2020). URL https://doi.org/10.1021/acs.nanolett.9b05092. Publisher: American Chemical Society.

[54] Zibrov, A. A. et al. Tunable interacting composite fermion phases in a half-filled bilayer-graphene Landau level. Nature **549**, 360–364 (2017).

[55] Weitz, R. T., Allen, M. T., Feldman, B. E., Martin, J. & Yacoby, A. Broken-Symmetry States in Doubly Gated Suspended Bilayer Graphene. Science (2010). URL https://science.sciencemag.org/content/early/2010/10/14/science.1194988.

[56] Bao, W. et al. Stacking-dependent band gap and quantum transport in trilayer graphene. Nature Physics **7**, 948–952 (2011). URL http://dx.doi.org/10.1038/nphys2103.

[57] Velasco, J. et al. Transport spectroscopy of symmetry-broken insulating states in bilayer graphene. Nature Nanotechnology **7**, 156–160 (2012). URL http://dx.doi.org/10.1038/nnano.2011.251.

[58] Liu, K. et al. Spontaneous broken-symmetry insulator and metals in tetralayer rhombohedral graphene. Nature Nanotechnology 1–8 (2023). URL https://www.nature.com/articles/s41565-023-01558-1.

[59] Han, T. et al. Correlated Insulator and Chern Insulators in Pentalayer Rhombohedral Stacked Graphene (2023). URL http://arxiv.org/abs/2305.03151. ArXiv:2305.03151 [cond-mat].

[60] Spanton, E. M. et al. Observation of fractional Chern insulators in a van der Waals heterostructure. Science **360**, 62–66 (2018). URL http://science.sciencemag.org/content/360/6384/62.

[61] Xie, Y. et al. Fractional Chern insulators in magic-angle twisted bilayer graphene. Nature **600**, 439–443 (2021). URL https://www.nature.com/articles/s41586-021-04002-3.

[62] Cai, J. et al. Signatures of fractional quantum anomalous hall states in twisted mote2. Nature **622**, 63–68 (2023).

[63] Shklovskii, B. I. & Efros, A. L. Electronic Properties of Doped Semiconductors (Springer, 1984).

[64] Büttiker, M. Negative resistance fluctuations at resistance minima in narrow quantum hall conductors. Physical Review B **38**, 12724 (1988).

[65] Kaverzin, A. A., Daimon, S., Kikkawa, T., Ohtsuki, T. & Saitoh, E. Negative longitudinal resistance of monolayer graphene in the quantum hall regime. Applied Physics Letters **124** (2024).

MATERIALS AND METHODS

Sample fabrication

Rhombohedral graphene, hBN and WS$_2$ flakes, are prepared by mechanical exfoliation on SiO$_2$/Si substrates. The identification of rhombohedral domain is accomplished through Raman spectroscopy using 488 nm wavelength, then verified with Bruker photothermal AFM-IR spectroscopy with finer resolution. The rhombohedral domain is subsequently isolated by AFM anodic oxidation to prevent conversion of rhombohedral to Bernal stacking order [32, 51].

The stacking process is divided into two steps. First, for devices A-C, hBN is picked up with a poly(bisphenol A carbonate) (PC) film and used to sequentially pick up a graphite bottom gate, hBN, and graphite (for contact material). The stack is then flipped with gold-coated PDMS-assisted flipping technique [52], resulting in a clean bottom part. Second, a graphite exfoliated on Polydimethylsiloxane (PDMS) is dropped on hBN, then picked up with suspended PC at $120\,^\circ$C, followed by the pick up of the rhombohedral graphene. Here we intentionally tried to align the straight edges of the hBN and the rhombohedral graphene in order to create the moiré superlattice. This top part is then dropped onto the bottom part and the PC is melted at $180\,^\circ$C. PC is washed with N-Methylpyrrolidone (NMP). After stacking, standard e-beam lithography and reactive-ion etching are utilized and Cr/Au is deposited for electrodes.

For device D, WS$_2$ layer is added for the bottom part to be at the top surface. In addition, when a rhombohedral graphene is picked up from the substrate and put down to the bottom stack, a negative 3-5 V was applied to the top gate while the silicon substrate and the rhombohedral graphene are grounded. The electrical connection to the top gate and the rhombohedral graphene is achieved by making an electrode on PC with gold stamping technique [52], before picking up the rhombohedral graphene. This strategy aims to promote hole-doping of the graphene, a condition known to favor rhombohedral stacking order [53].

Device characterization and measurements

Electrical transport and penetration field capacitance measurements are performed in a dilution refrigerator, at the base temperature of $\sim 15\,\mathrm{mK}$ unless otherwise specified. Notably, compressibility measurements are sensitive to impedances on the $Z \sim 100\,\mathrm{M\Omega}$ scale, making them tolerant to the high contact resistances in our devices at large D, which preclude transport measurements in this regime (see Fig. ED1e-f). Four-terminal resistance is measured using lock-in amplifiers (Stanford Research Systems, SR860) with current amplifier (Basel Precision Instruments, SP983), with typical AC excitations of $0.5 - 2\,\mathrm{nA}$ at 17.777 Hz. $n_e = (c_{tg}V_{tg} + c_{bg}V_{bg})/e$ and $D = (c_{tg}V_{tg} - c_{bg}V_{bg})/2\epsilon_0$ are calibrated by finite magnetic field Landau levels at electron doped side ($n_e > 0$) around $D = 0\,\mathrm{V/nm}$, where c_{tg} and c_{bg} are the geometric capacitances per area of the top and bottom gates, e is the elementary charge, and ϵ_0 is the vacuum permittivity.

To measure the penetration field capacitance of the sample, we utilized high electron mobility transistor (HEMT) as described in Ref. [23]. Calibration of the capacitance into inverse compressibility $\kappa = \partial\mu/\partial n_e$ is achieved by balancing the capacitance circuit when the sample is at two different limits (metallic and insulating) as references, as described in Ref. [54]. Uncalibrated κ is sometimes used when the interest of the measurement is only to reveal the contrast between different states. We limit the bias current through the HEMT in order to minimize the Joule heating, especially when it matters for measuring temperature dependencies of CI and FCI (Fig. 3e,f). We checked that the superconducting pocket is not affected with HEMT operating, implying the effective temperature is still close to the base temperature. Note that since devices A-C share the same top and bottom gates (see Fig. ED1), our measurement of capacitance sums all three devices. However, the phase diagrams of individual devices from transport are nearly identical (see Fig.ED12), hence mainly improving the signal to noise ratio in capacitance.

Due to the device geometry, Hall resistance measured by the configurations $R_{13,24}$ and $R_{24,13}$ shown in Fig. ED11 often capture R_{xx} components. However, the measured $R_{13,24}$ is equal to R_{xy} in the quantum anomalous Hall regime, showing good quantization without any symmetrization process since R_{xx} drops to zero in the regime. We plot the Onsager (anti-)symmetrized $R_{xx} = (R_{14,23} + R_{23,14})/2$ and $R_{xy} = (R_{13,24} - R_{24,13})/2$ only when finite R_{xx} and geometric mixing hinders clear explanation (Fig. 1d-f, Fig. ED3a,b,e, and Fig. ED7). We plot the raw resistances from configurations $R_{xx} = R_{14,23}$ and $R_{xy} = R_{13,24}$ in the rest of the paper. When taking magnetic field hysteresis for QAH at $\nu = -1$, n_e is tuned with B_z to compensate the slope from the non-zero Chern number and to stay in the QAH state (Fig. 1e,f, Fig. ED3a,b, and Fig. ED11.

Entering a valley-polarized state from a state with no polarization causes line-by-line switching events in two-dimensional data, as can be seen in Fig.4a, Fig.ED3a-c, Fig.ED4b, Fig.ED5a, and Fig.ED8a. This behavior can be attributed to magnetic domains, as occur when ferromagnetic states are 'zero-field cooled'. Since states of opposite valley polarization are degenerate at zero magnetic field, entering a valley polarized state as a function of gates is expected to lead to an arbitrary choice of one of the degenerate configurations. As in ferromagnets, other, multi-domain configurations may also be close enough in energy that they can be stabilized if the transition is crossed faster than the relevant relaxation time. Notably, states with different valley polarization have different R_{xy}, while multi-domain states will have different R_{xx} as well. As a result, repeated quenching into

the polarized state (as happens between lines) can stabilize states with different measured transport properties, which resemble line-by-line switching noise in the data. This switching noise reflects different microscopic polarizations of the valley moments, and is suppressed by applied magnetic field, which favors a uniform polarization into a single valley.

Pauli-limit violation ratio of ABCA and ABCA/WS$_2$ devices

We compare the Pauli-limit violation ratio (PVR) between the hBN encapsulated ABCA (device A) and spin-orbit proximitized ABCA/WS$_2$ device (device D). The measured $B_{c,\parallel}$ at the base temperature is divided by the Pauli-limit $B_p = 1.86 \times T_c$ (T_c taken at zero field) for BCS superconductor, and define PVR $= B_{c,\parallel}/B_p$. The raw data for the extraction can be found in Fig. ED4b and c for SC in ABCA, and Fig. 4b,c, Fig. ED9d,f for SC1 and SC2 in ABCA/WS$_2$.

Without spin-orbit coupling, PVR from SC in ABCA (Fig. ED4g) is around 1 or less as a function of doping, showing agreement with BCS theory. SC1 from ABCA/WS$_2$ (which occurs at a similar position to SC in ABCA) shows significantly improved PVR due to the spin-orbit coupling (Fig. ED9e). Interestingly, SC2 from ABCA/WS$_2$ does not show an improvement of PVR (Fig. ED9k).
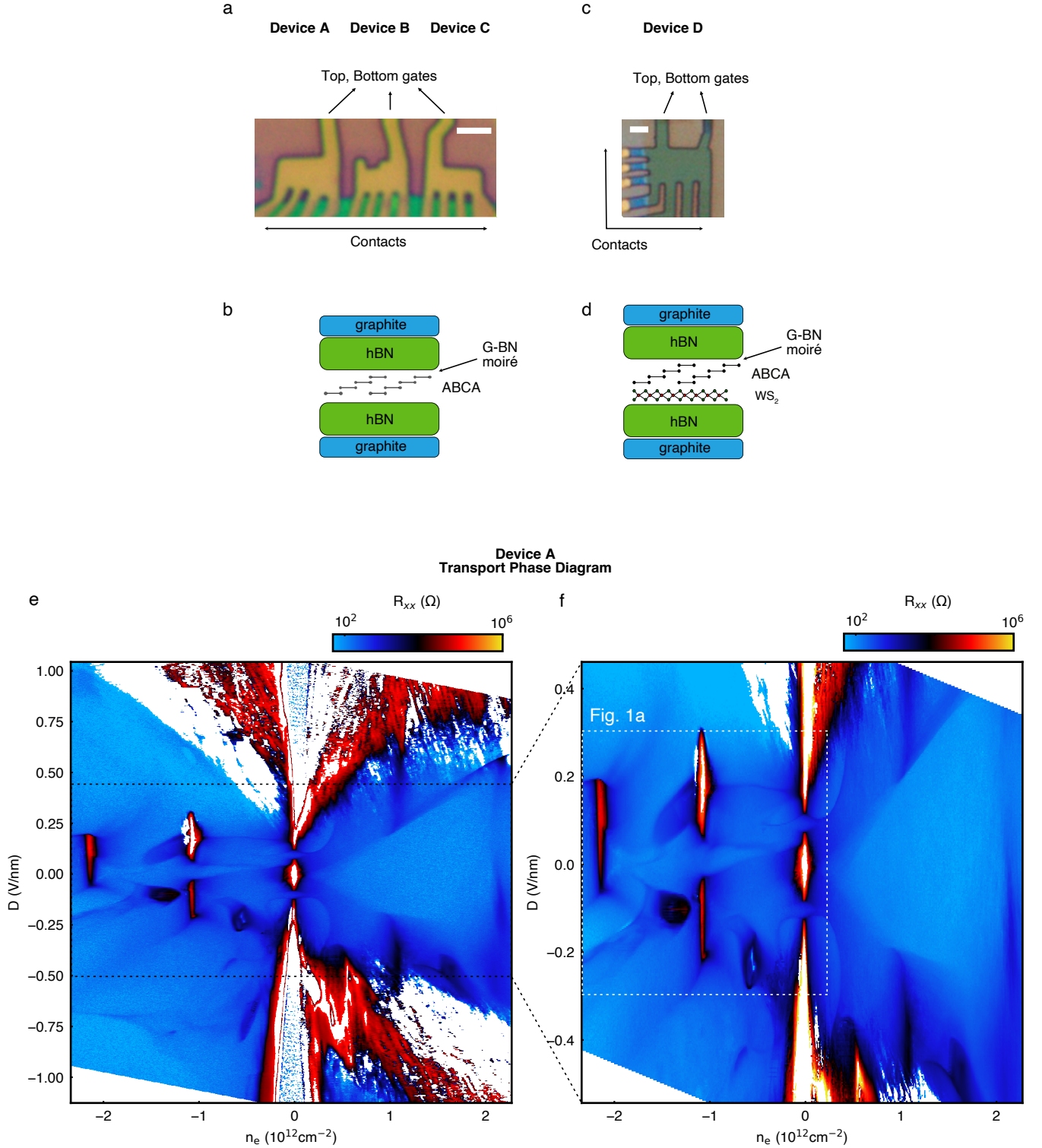
EXTENDED DATA

a Device A   Device B   Device C

Top, Bottom gates

Contacts

b

graphite
hBN
G-BN moiré
ABCA
hBN
graphite

c Device D

Top, Bottom gates

Contacts

d

graphite
hBN
G-BN moiré
ABCA
WS$_2$
hBN
graphite

Device A
Transport Phase Diagram

e R_{xx} (Ω)

10^2 10^6

D (V/nm)

n_e (10^{12}cm^{-2})

f R_{xx} (Ω)

10^2 10^6

Fig. 1a

D (V/nm)

n_e (10^{12}cm^{-2})

FIG. ED1. **Optical images and schematics of the devices, and large range transport phase diagram from Device A. a**, Optical microscope image of the ABCA devices A, B, and C. They all share the common top and bottom gates, hence the penetration capacitance measurement sums the signals from the three devices. Device A is where the main text transport data are taken. Scale bar: $2\,\mu$m. **b**, Schematic of the devices A-C. **c**, Image of the ABCA/WS$_2$ device D with the scale bar of $2\,\mu$m. **d**, Schematic for device D. **e, f**, Large range transport phase diagrams from device A. Electrical contact issues prevent measuring states at high $|D|$. The range where Fig. 1a is taken is outlined in **f**. At charge neutrality, we observe an insulating phase at high $|D|$ associated with a layer-polarized state and a distinct insulator near $D = 0$ associated with a layer-antiferromagnet [55–59]. Additional insulating states at $\nu = -2$ are also observed, arising from the spontaneous formation of isospin polarized correlated insulating states [38].
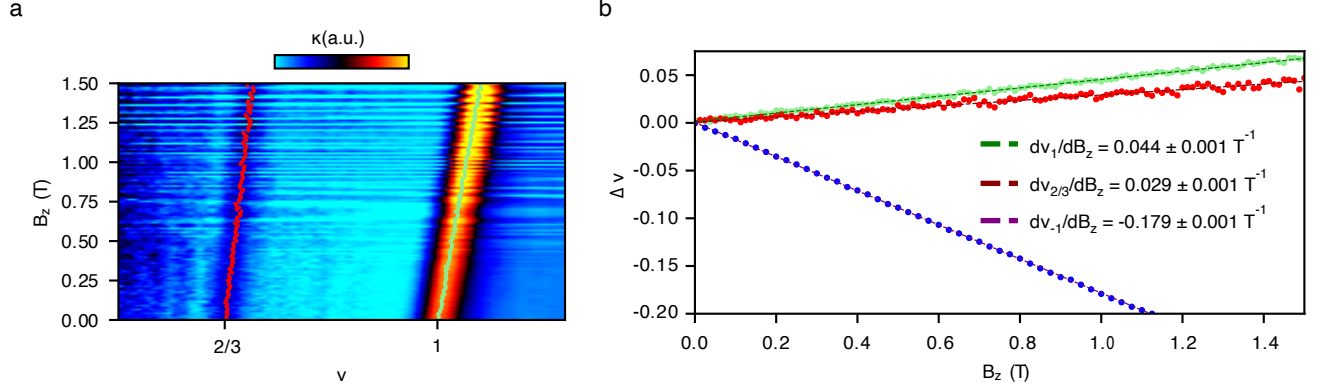
FIG. ED2. **Extraction of Chern numbers from capacitance. a,** Magnetic field dependence of κ for $\nu = 1$ and $2/3$ at $D = 0.885\,\mathrm{V/nm}$. The red dots denote the peak position corresponding to the incompressible state appearing at $\nu = 2/3$ when B=0, while the green dots correspond to the peak position for the $\nu = 1$. **b,** Variation of the moire filling, $\Delta\nu(B)$ for the three incompressible states as determined from the data plotted in panel **a** and Fig. 3**b** . The dashed lines represent linear fits, with the slopes indicated in the legend. The Chern numbers can be extracted from the Streda formula $C = \frac{\Phi_0}{A_{uc}}\frac{d\nu}{dB} = \Phi_0\frac{|n_{\pm 4}|}{4}\frac{d\nu}{dB}$; with A_{uc} the area of moire unit cell and $n_{\pm 4}$ the carrier density at $\nu = \pm 4$. The obtained $C(\nu = 1) = 0.98 \pm 0.03$, $C(\nu = 2/3) = 0.64 \pm 0.03$, and $C(\nu = -1) = -4.0 \pm 0.1$ are consistent with the expected Chern numbers 1, 2/3, and -4, respectively, assuming $|n_{\pm 4}| = (2.15 \pm 0.05) \times 10^{12}\,\mathrm{cm}^{-2}$ (determined by quantum oscillations at $D = 0$). Fractional Chern insulator were also found in [37, 60–62]
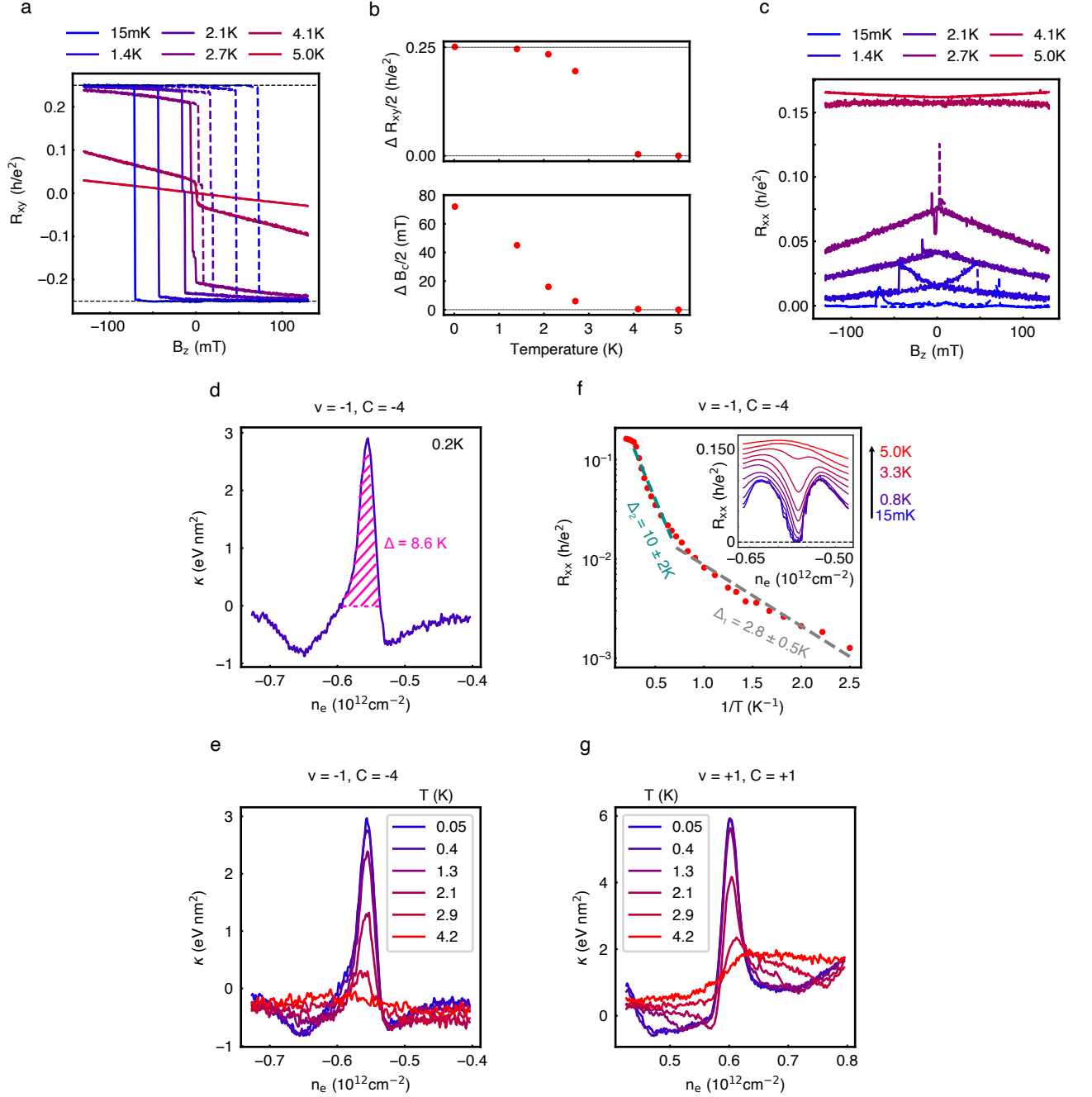
FIG. ED3. **Energetics of QAH at $\nu = -1$ and $\nu = +1$. a-c**, Temperature dependence of hysteresis loops of R_{xy} (**a**) and R_{xx} (**c**) taken at $n_e = -0.564 \times 10^{12}\,\mathrm{cm}^{-2}$ (when $B_z = 0$), showing the Curie temperature $T_{\mathrm{Curie}} \approx 4.5\,\mathrm{K}$. Panel **b** summarizes $\Delta R_{xy}/2$ ($B_z = 0$) (upper) and coercive field (lower) from **a** as a function of temperature for clarity. **d**, Gap determination from κ, showing the case of $\nu = -1$ Chern insulator. We integrate $\kappa = \partial\mu/\partial n_e$ above zero over the incompressible peak to estimate the chemical potential jump. **e**, T dependence of κ for $\nu = -1$ Chern insulator. **f**, Activation gap measurement of the QAH state at $\nu = -1$. The inset shows the temperature dependence of R_{xx} as a function of n_e around the quantized region of QAH. The dip at low temperature corresponding to QAH regime fills up as T increases. The main panel shows temperature dependence of R_{xx} inside of the dip (at the same position as **a** and **c**). The activation gap Δ can be obtained by the Arrhenius fitting following $R_{xx} \sim e^{-\Delta/(2T)}$. We find around a decade of linear activation for different temperature ranges, which gives $\Delta_1 = 2.8 \pm 0.5\,\mathrm{K}$ for low temperature and $\Delta_2 = 10 \pm 2\,\mathrm{K}$ for intermediate temperature regimes. Δ_2 agrees better to the measured thermodynamic gap from **d**. We interpret the smaller gap (Δ_1) extracted at lower temperature as arising from disorder-mediate hopping[63].

a-f are taken at $D = -0.208\,\mathrm{V/nm}$. **g**, T dependence of κ for $\nu = +1$ Chern insulator at $D = 0.835\,\mathrm{V/nm}$.
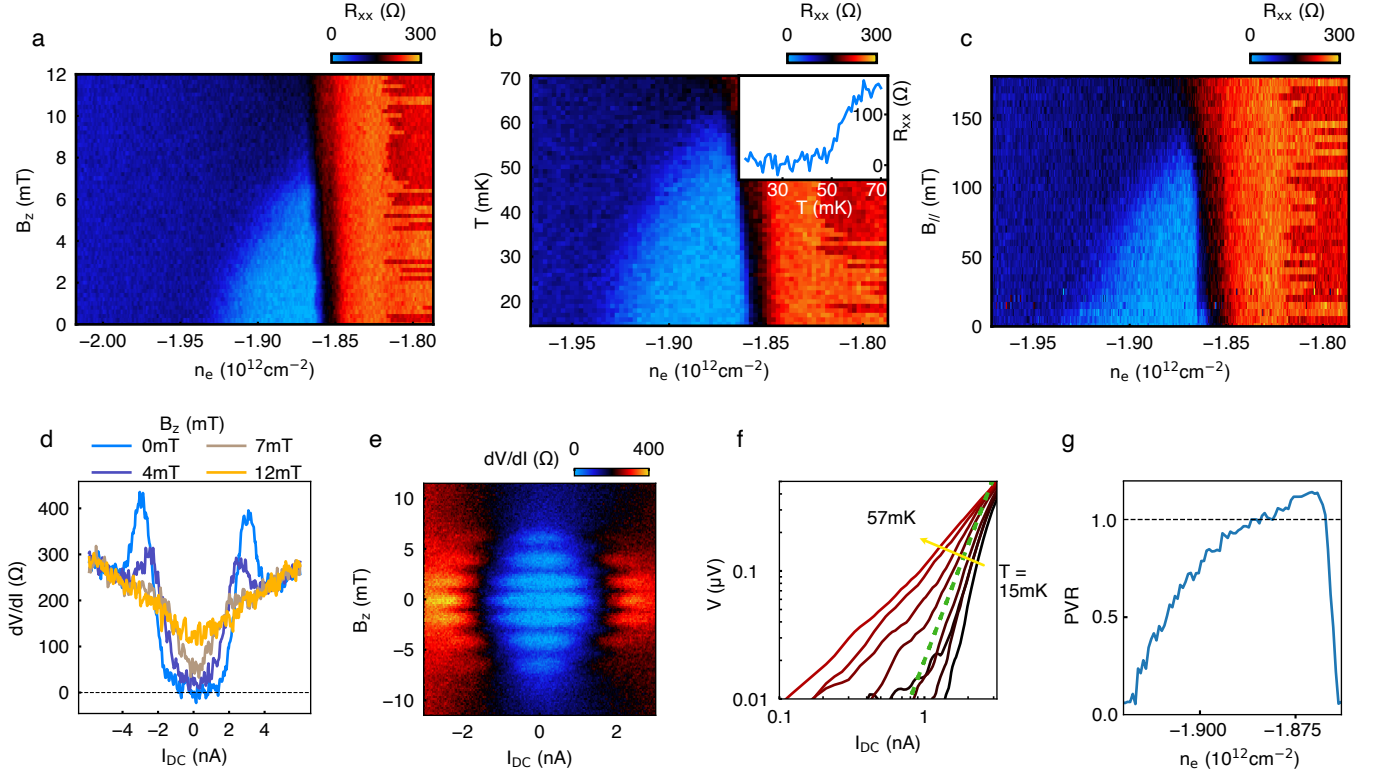
FIG. ED4. **Characterization of the superconductivity. a-c**, R_{xx} as a function of electron density n_e and out-of-plane field B_z (**a**), temperature T (**b**), and in-plane field $B_\parallel$ (**c**). Inset of **b** shows R_{xx} vs T at the optimal $n_e = -1.868 \times 10^{12}$ cm^{-2}. **d**, B_z dependent dV/dI vs I_{DC} at $n_e = -1.879 \times 10^{12}$ cm^{-2}, $D = -0.138$ V/nm. **e**, B_z dependent dV/dI at $n_e = -1.865 \times 10^{12}$ cm^{-2}, close to the right-side boundary of the superconducting pocket. Oscillation due to macroscopic interference is observed, corroborating coherence of the superconducting state. **f**, Temperature dependent V vs I_{DC} taken at $n_e = -1.879 \times 10^{12}$ cm^{-2}. The green dashed line indicates where $V \propto I^3$, showing $T_{BKT} \approx 40$ mK. **g**, Pauli limit violation ratio (PVR) as a function of n_e, showing overall obedience of the Pauli limit (see Methods for the discussion). All data here are taken at $D = -0.138$ V/nm.
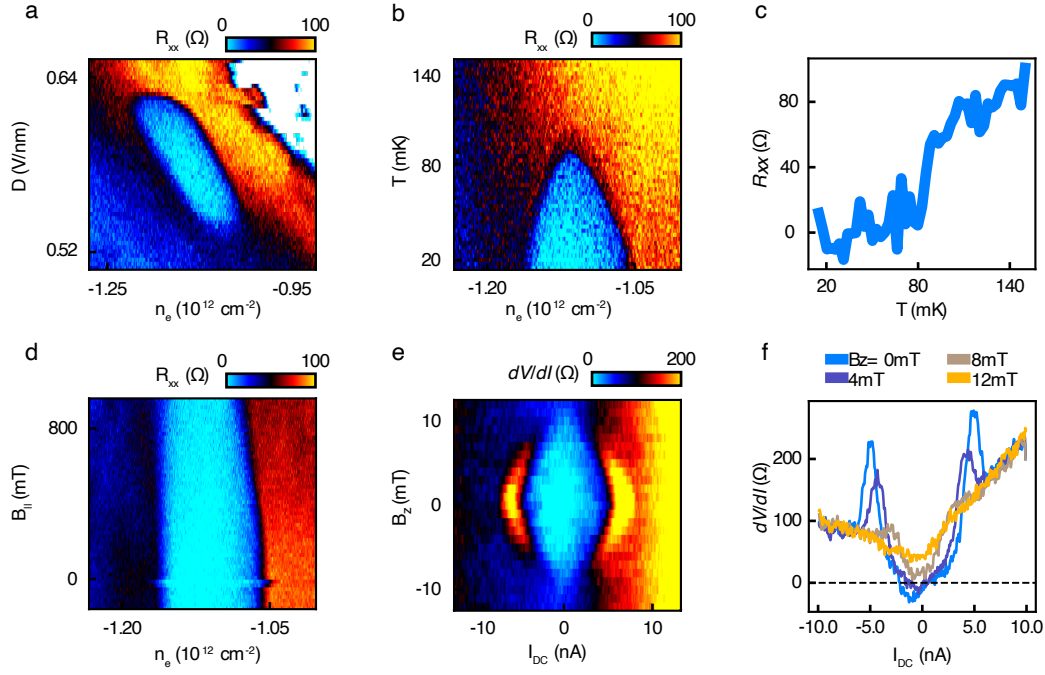
FIG. ED5. **Characterization of superconductivity for strong moiré potential Device A. a**, (n_e, D) phase diagram of R_{xx} around the superconducting pocket on the strong moiré side. The white region of the phase diagram indicates where the contact resistance becomes too large for transport measurements. **b**, R_{xx} as a function of T and n_e taken at $D = 0.576$ V/nm. **c**, R_{xx} vs T at $n_e = -1.125 \times 10^{12}$ cm^{-2}. **d**, In plane field dependence, R_{xx} as a function of $B_\parallel$ and n_e taken at $D = 0.576$ V/nm. **e, f**, dV/dI as a function of B_z and I_{DC} at $n_e = -1.123 \times 10^{12}$ cm^{-2} and $D = 0.576$ V/nm. The measured critical current $I_c \approx 5$ nA, while the critical out-of-plane field B_c is 10 mT.
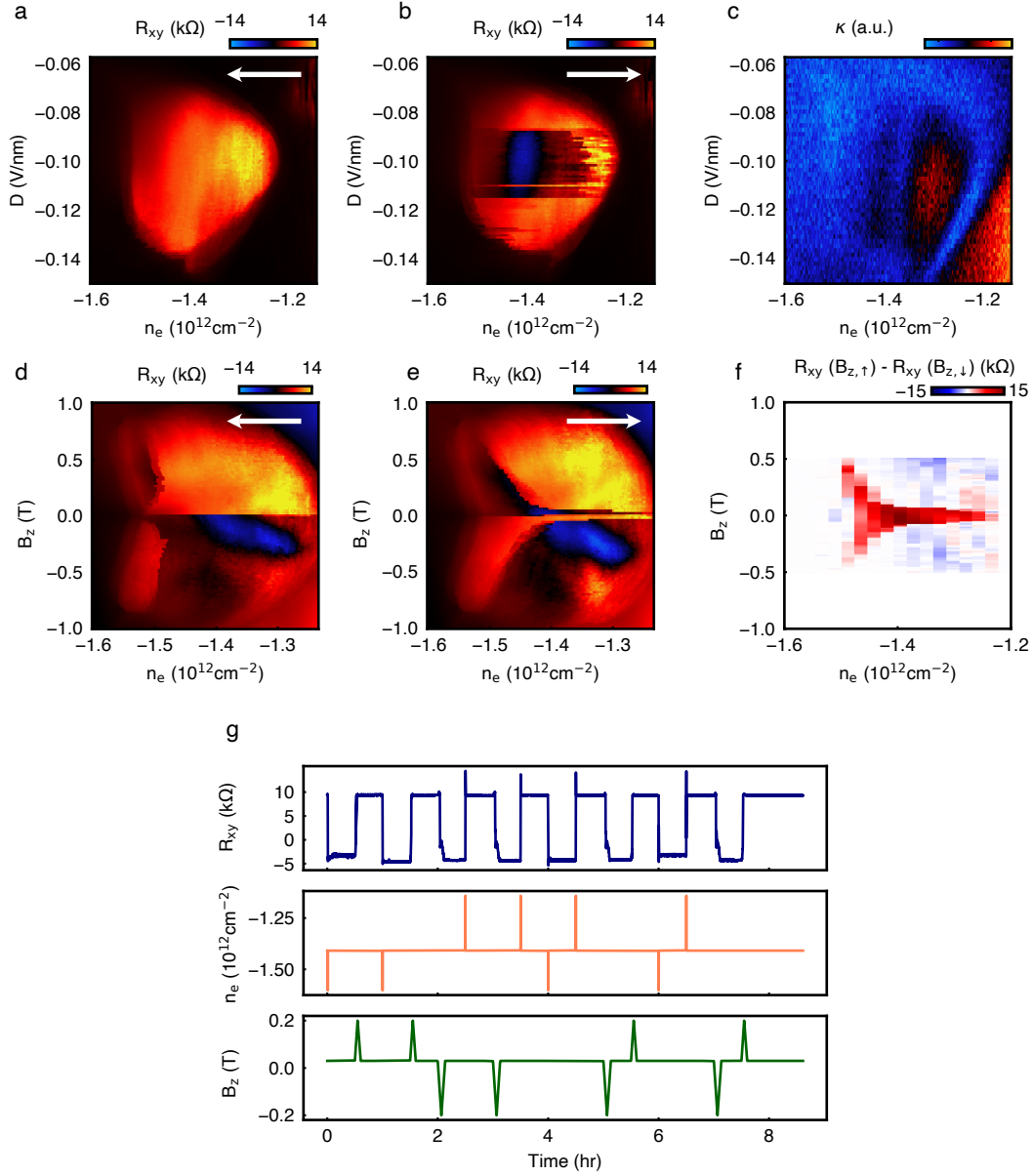
FIG. ED6. **Anomalous Hall effect and electrical switching around $\nu \sim -2.5$. a**, (n_e, D) dependent R_{xy} at $B_z = 30\,\text{mT}$ with n_e as the fast sweep axis from right to left. **b**, same as (**a**) but with the opposite sweep direction. **c**, $\kappa = \partial\mu/\partial n_e$ from the penetration capacitance at the same range as **a** and **b**. **d**, **e**, (n_e, B_z) dependent R_{xy} with different sweep directions in n_e. The magnetic moment m of the state changes sign around $n_e = -1.5 \times 10^{12}\,\text{cm}^{-2}$ when B_z is around zero, and the mechanism of the electrical switch is similar to the mechanism discussed in Fig. 2. **f**, Resistance difference between R_{xy} when sweeping up in B_z and R_{xy} sweeping down in B_z. **g**, Non-volatile switching of the two states, controlled by B_z and n_e. **d-g** are taken with $D = -0.102\,\text{V/nm}$. All data here are taken at 200 mK.
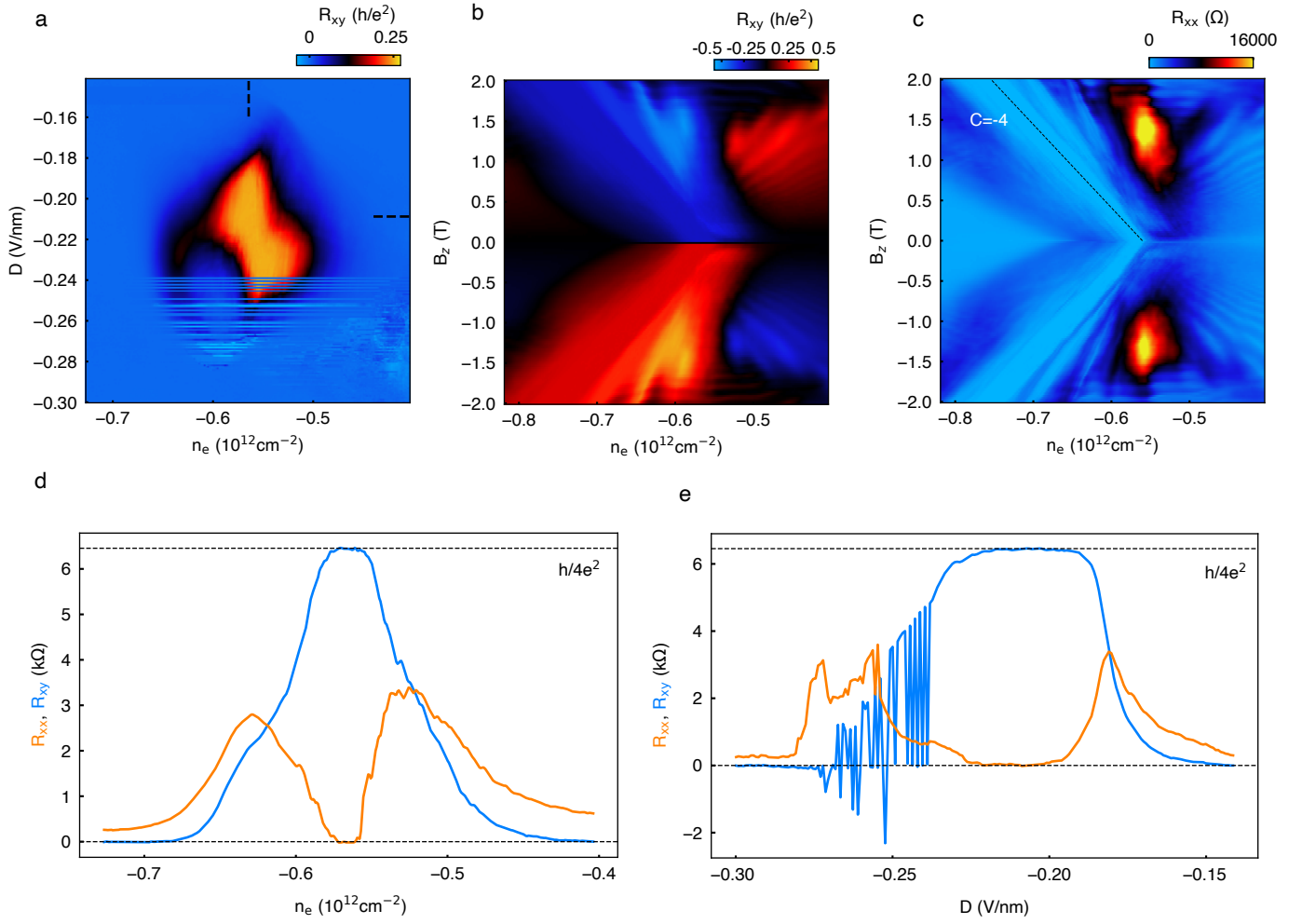
FIG. ED7. **Landau fans and stability of quantization in QAH state at** $\nu = -1$. **a**, (n_e, D) dependent R_{xy} around QAH state with n_e as the fast sweep axis. The switching behavior indicates the closeness of the two states in energy. The dashed lines are the positions where **d** and **e** are taken. **b**, R_{xy} Landau fan, showing a plateau along the $|C| = 4$ slope. **c**, R_{xx} Landau fan, where the dashed line correspond to $|C| = 4$ from Streda formula. Both fans are taken at $D = -0.208\,\mathrm{V/nm}$. **d**, Linecuts with constant $D = -0.208\,\mathrm{V/nm}$, showing quantized R_{xy} around the value $h/4e^2$ and R_{xx} around zero. **e**, Linecuts with constant $n_e = -0.564 \times 10^{12}\,\mathrm{cm}^{-2}$.
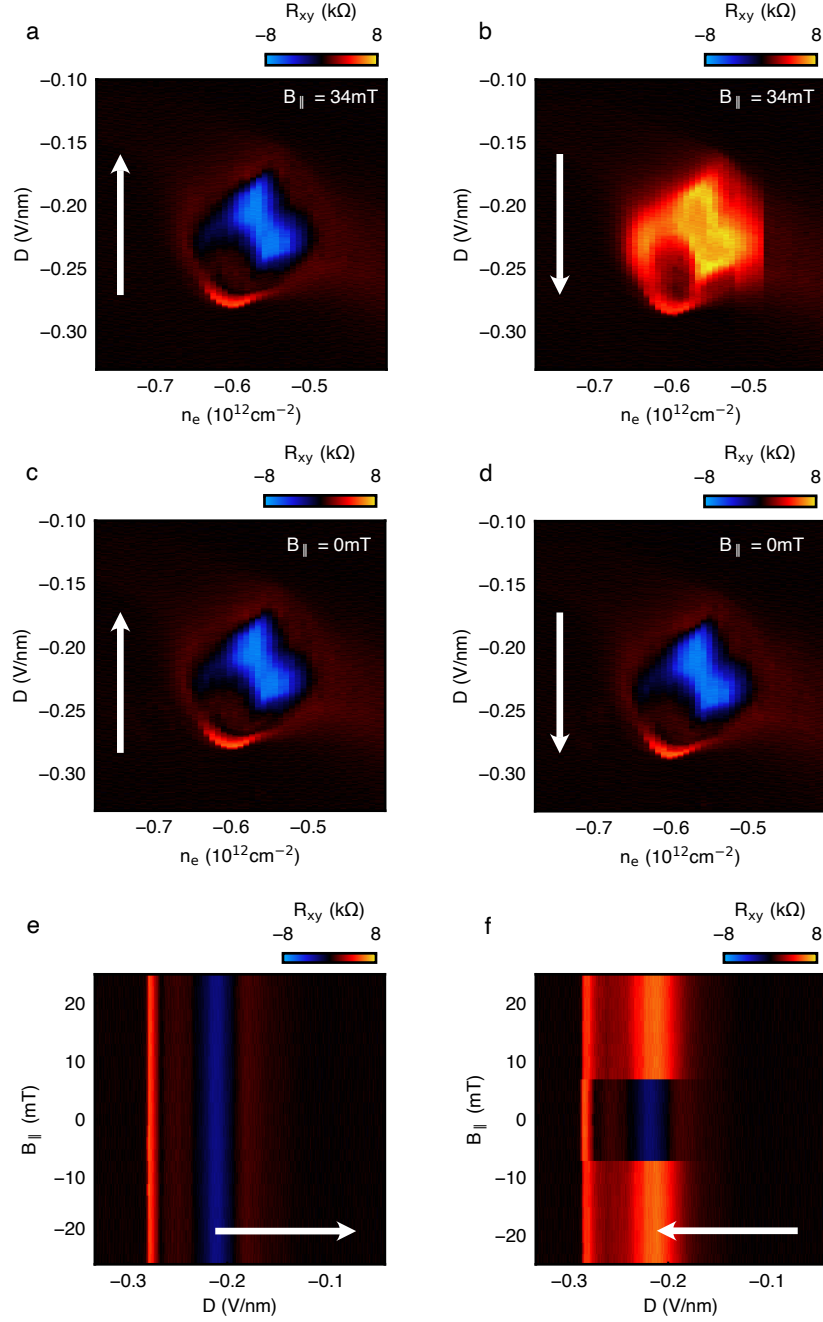
FIG. ED8. **In-plane magnetic field dependence of electric switching at** $\nu = -1$. **a, b,** (n_e, D) dependent R_{xy} at $B_\parallel = 34\,\mathrm{mT}$, D as the fast sweep axis. Sweep direction is indicated in the arrows. At sufficiently large $B_\parallel$, the electrical switching exists. **c, d,** Same as **a** and **b**, but $B_\parallel = 0\,\mathrm{mT}$. The switching is not present. **e, f,** $B_\parallel$ dependence of the switching at a fixed $n_e = -0.607 \times 10^{12}\,\mathrm{cm}^{-2}$. A small but finite $B_\parallel$ is required in order to observe switching. The data here are taken with nominal $B_z = 5\,\mathrm{mT}$.
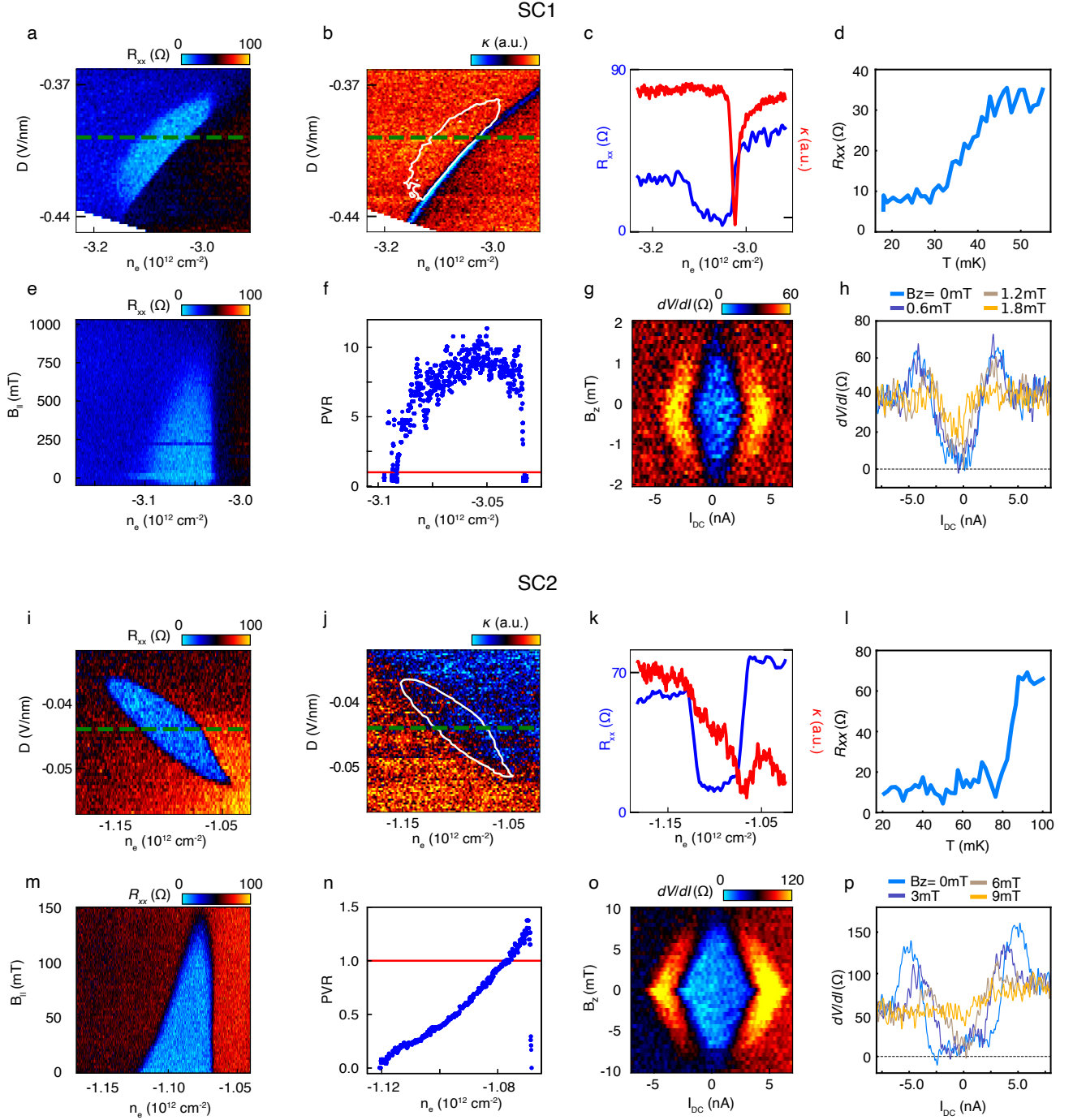
FIG. ED9. **Characterization of superconductivity SC1 and SC2 in ABCA/WS$_2$ device D. a**, (n_e, D) phase diagram of R_{xx} around the superconducting pocket SC1. **b**, Inverse compressibility κ measured around SC1. White contour indicates the superconducting region extracted from **a**. The dashed line is at $D = -0.399$ V/nm, where **c-h** are taken. **c**, Linecuts of R_{xx} (blue) and κ (red) for SC1, where a clear dip of κ is visible on the right side of the superconducting region suggesting a first-order phase transition. **d**, R_{xx} vs T at $n_e = -3.049 \times 10^{12}$ cm^{-2}. **e**, $B_\parallel$ dependence of SC1. **f**, PVR for SC1 as a function of doping, showing a huge improvement compared to the case of ABCA device without WS$_2$. **g, h**, dV/dI as a function of B_z and I_{DC} at $n_e = -3.051 \times 10^{12}$ cm^{-2}, manifesting critical current $I_c \approx 2$ nA and critical field B_c around 1.5 mT. **i, j**, n_e, D phase diagram of R_{xx} and κ of SC2. **k**, R_{xx} and κ linecuts, with κ showing a slight dip on the right side of the superconducting region. **l**, R_{xx} vs T at $n_e = -1.092 \times 10^{12}$ cm^{-2}. **m, n**, $B_\parallel$ dependence and PVR of SC2 showing overall obedience of the Pauli limit. **o, p**, dV/dI as a function of B_z and I_{DC} at $n_e = -1.104 \times 10^{12}$ cm^{-2}, $D = -0.043$ V/nm, with $I_c \approx 3$ nA and $B_c \approx 8$ mT.
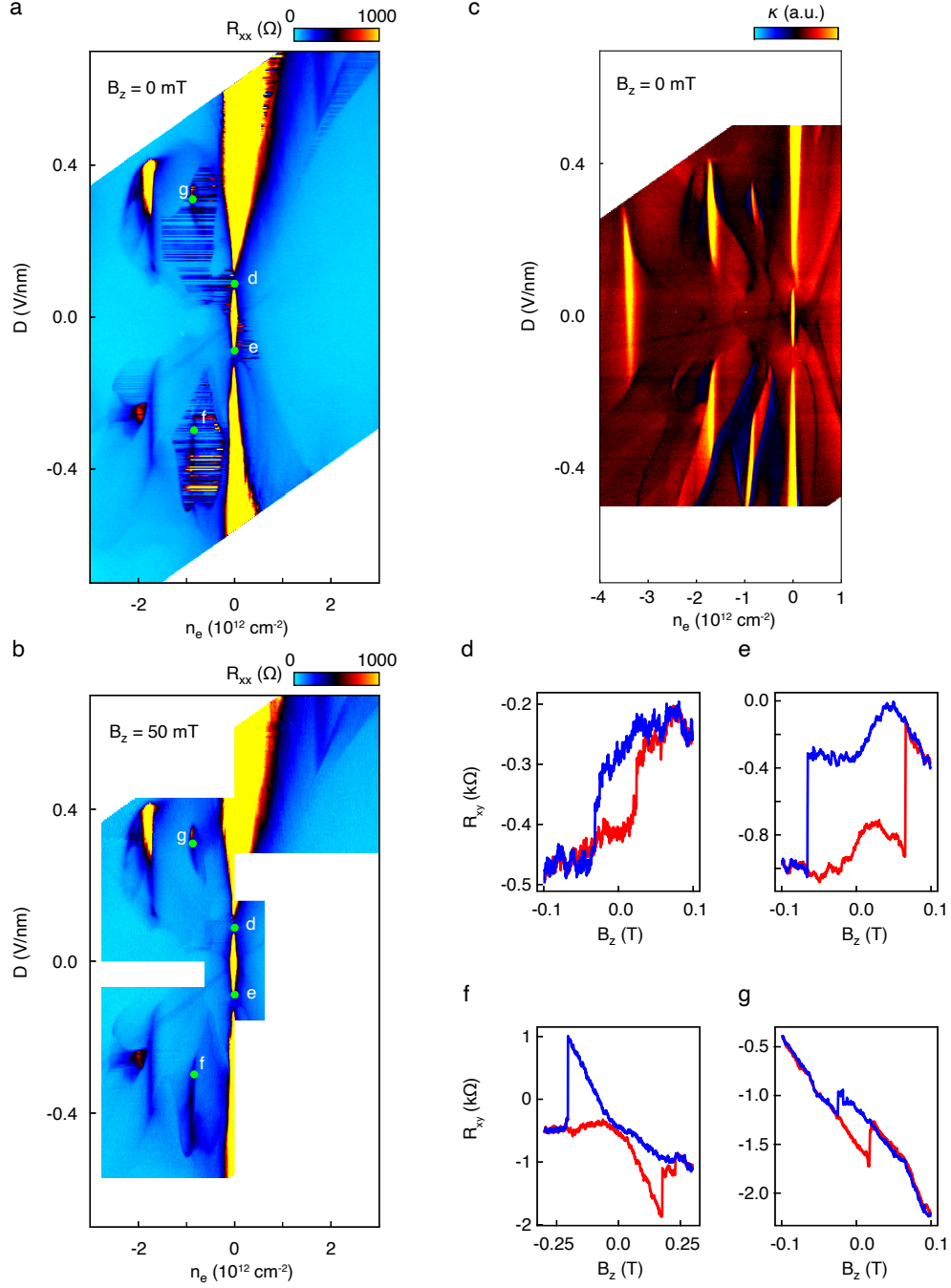
FIG. ED10. **Phase diagram and anomalous Hall effect in ABCA/WS$_2$ device D. a**, (n_e, D) dependent R_{xx} at zero magnetic field. Several switchy regions are observed. **b**, Switchy behavior is suppressed by a small out-of-plane magnetic field of $B_z = 50\,\text{mT}$. This is consistent with a magnetic origin, with bistability caused by different orbital magnetization states. **c**, (n_e, D) dependent penetration capacitance at zero magnetic field. **d-g**, R_{xy} hysteresis loops as a function of B_z. **d** and **e** are at $\nu = 0$ and **f** and **g** are at $\nu = -1$, as marked in **a** and **b**.
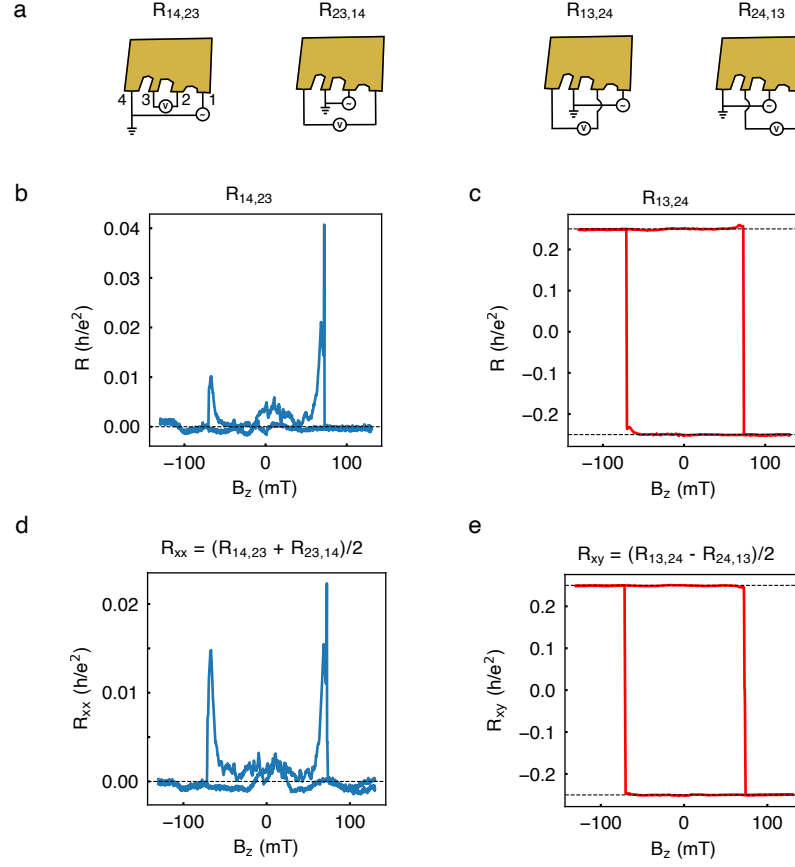
FIG. ED11. **Onsager (anti-)symmetrization. a**, Contact configuration $R_{14,23}$ and its Onsager pair $R_{23,14}$ for R_{xx} measurement, and $R_{13,24}$ and its Onsager pair $R_{24,13}$ for R_{xy} measurement. **b-e**, Process to obtain Fig. 1e and f. Resistances from $R_{14,13}$ and $R_{13,24}$ contact configurations are shown in **b** and **c**, roughly corresponding to R_{xx} and R_{xy} each and already showing good quantization since R_{xx} goes to zero in QAH, minimizing the geometrical mixing. **d** and **e** are obtained by Onsager symmetrization, showing less deviation from the quantized value, particularly at B_z around the coercive fields where the R_{xx} becomes large and the geometrical mixing presents. In the quantum anomalous Hall phase, we find $R_{xx} < 0$, which may be associated with coupling of edge modes via localized states [64, 65].
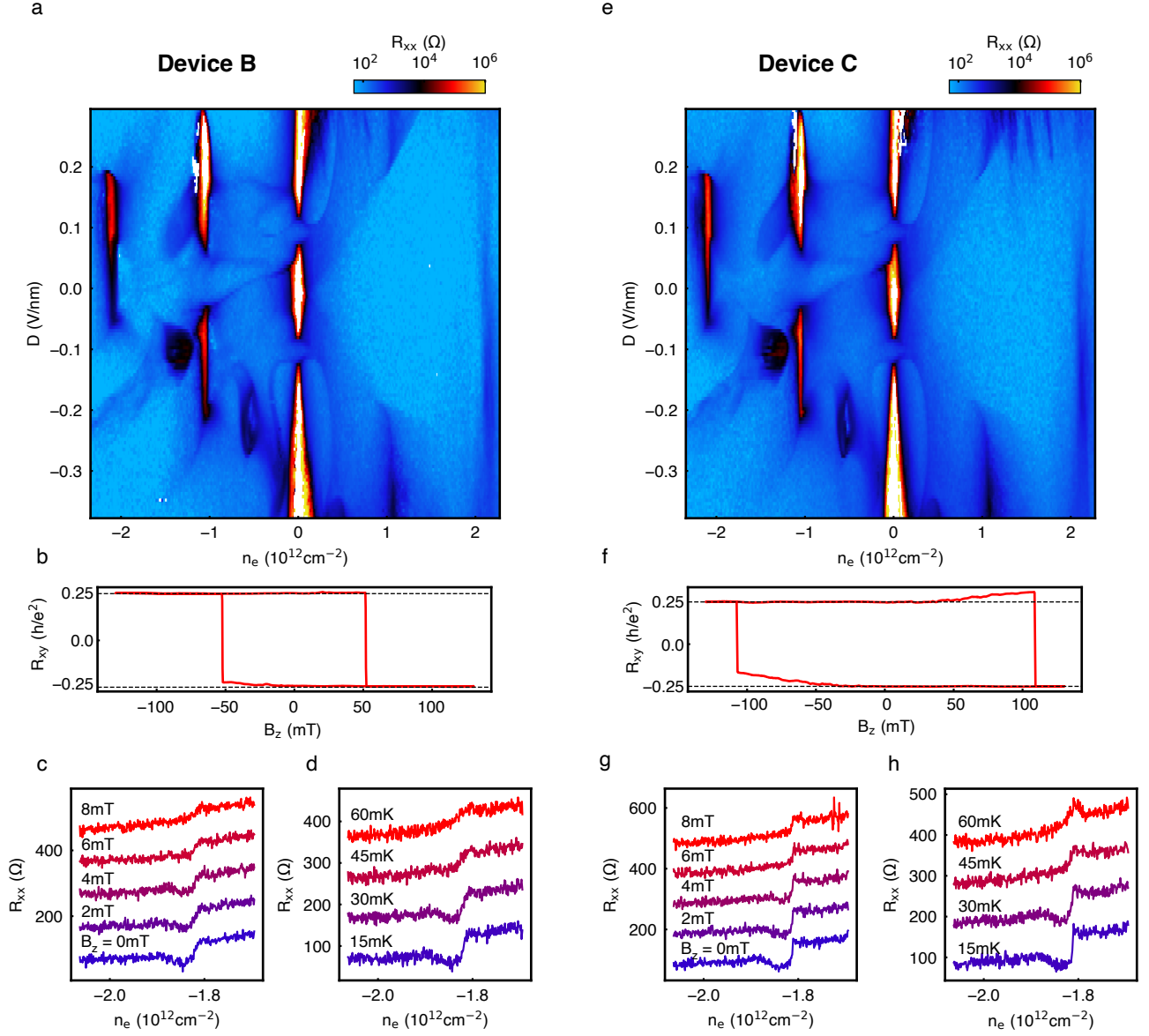
FIG. ED12. **Reproducibility, signatures of superconductivity and QAH states in devices B and C. a,** (n_e, D) dependent R_{xx} in device B, showing the same features at nearly identical positions with device A. **b,** Hysteresis loop of R_{xy} for the QAH state in device B taken at $n_e = -0.558 \times 10^{12}$ cm^{-2} and $D = -0.208$ V/nm, showing a good quantization around $h/4e^2$. **c, d,** B_z and temperature dependence of R_{xx} along the linecut at $D = -0.131$ V/nm, crossing the signature of superconductivity. The critical field and temperature values from the resistance dip are similar to the superconductivity in device A, despite the fact that the resistance does not drop to zero due to the mixing of filtering grounds for different contacts in devices B and C. Curves are offset by 100Ω for clarity. **e-h,** Dataset from Device C. (n_e, D) dependent R_{xx} (**e**), R_{xy} hysteresis loop for QAH state taken at $n_e = -0.562 \times 10^{12}$ cm^{-2} and $D = -0.208$ V/nm (**f**), B_z and T dependence of R_{xx} for the superconducting state taken at $D = -0.131$ V/nm (**g**).

Supplementary Information for Electric field control of superconductivity and quantized anomalous Hall effects in rhombohedral tetralayer graphene

Youngjoon Choi,[1, *] Ysun Choi,[1, *] Marco Valentini,[1, *] Caitlin L. Patterson,[1] Ludwig F. W. Holleis,[1] Owen I. Sheekey,[1] Hari Stoyanov,[1] Xiang Cheng,[1] Takashi Taniguchi,[2] Kenji Watanabe,[3] and Andrea F. Young[1, †]

[1]*Department of Physics, University of California at Santa Barbara, Santa Barbara, California 93106, USA*
[2]*Research Center for Materials Nanoarchitectonics, National Institute for Materials Science, 1-1 Namiki, Tsukuba 305-0044, Japan*
[3]*Research Center for Electronic and Optical Materials, National Institute for Materials Science, 1-1 Namiki, Tsukuba 305-0044, Japan*

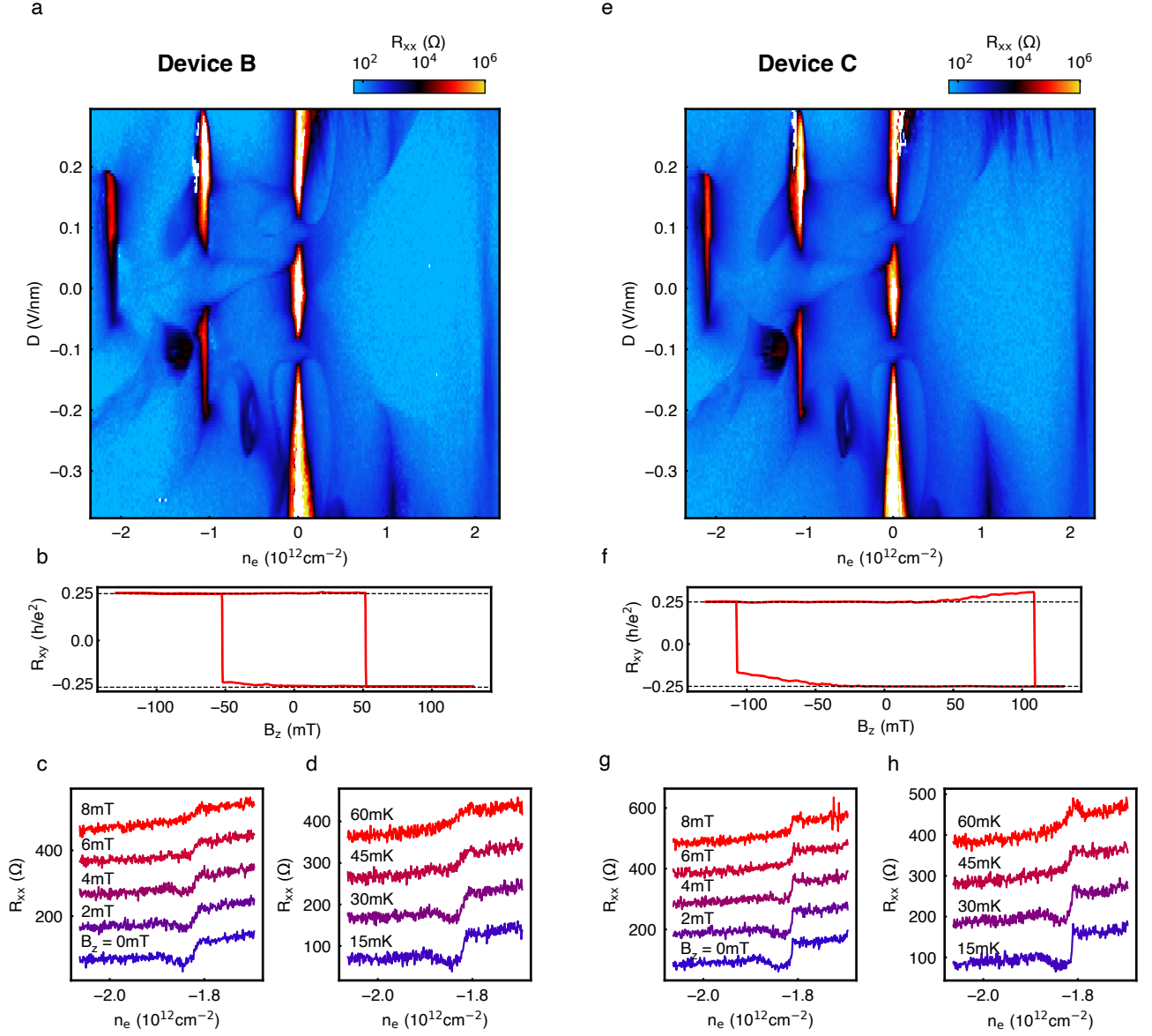(Dated: April 16, 2025)

Supplementary information

FIG. S1. **Reproducibility, signatures of superconductivity and QAH states in devices B and C. a,** (n_e, D) dependent R_{xx} in device B, showing the same features at nearly identical positions with device A. **b,** Hysteresis loop of R_{xy} for the QAH state in device B taken at $n_e = -0.558 \times 10^{12}$ cm^{-2} and $D = -0.208$ V/nm, showing a good quantization around $h/4e^2$. **c, d,** B_z and temperature dependence of R_{xx} along the linecut at $D = -0.131$ V/nm, crossing the signature of superconductivity. The critical field and temperature values from the resistance dip are similar to the superconductivity in device A, despite the fact that the resistance does not drop to zero due to the mixing of filtering grounds for different contacts in devices B and C. Curves are offset by 100Ω for clarity. **e-h,** Dataset from Device C. (n_e, D) dependent R_{xx} **(e)**, R_{xy} hysteresis loop for QAH state taken at $n_e = -0.562 \times 10^{12}$ cm^{-2} and $D = -0.208$ V/nm **(f)**, B_z and T dependence of R_{xx} for the superconducting state taken at $D = -0.131$ V/nm **(g)**.
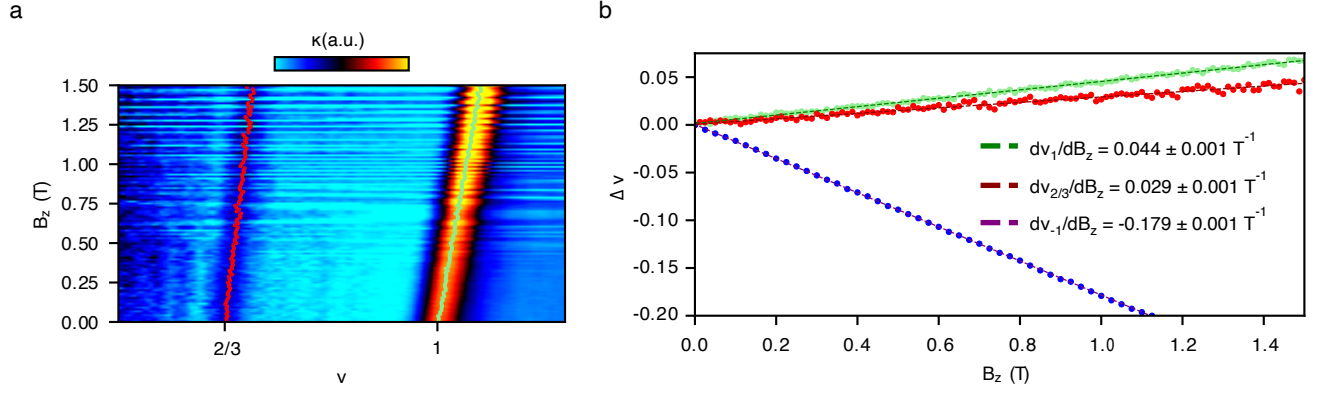
FIG. S2. **Extraction of Chern numbers from capacitance. a**, Magnetic field dependence of κ for $\nu = 1$ and $2/3$ at $D = 0.885\,\mathrm{V/nm}$. The red dots denote the peak position corresponding to the incompressible state appearing at $\nu = 2/3$ when B=0, while the green dots correspond to the peak position for the $\nu = 1$. **b**, Variation of the moire filling, $\Delta\nu(B)$ for the three incompressible states as determined from the data plotted in panel **a** and Fig. 3**b** . The dashed lines represent linear fits, with the slopes indicated in the legend. The Chern numbers can be extracted from the Streda formula $C = \frac{\Phi_0}{A_{uc}}\frac{d\nu}{dB} = \Phi_0 \frac{|n_{\pm 4}|}{4}\frac{d\nu}{dB}$; with A_{uc} the area of moire unit cell and $n_{\pm 4}$ the carrier density at $\nu = \pm 4$. The obtained $C(\nu = 1) = 0.98 \pm 0.03$, $C(\nu = 2/3) = 0.64 \pm 0.03$, and $C(\nu = -1) = -4.0 \pm 0.1$ are consistent with the expected Chern numbers 1, 2/3, and -4, respectively, assuming $|n_{\pm 4}| = (2.15 \pm 0.05) \times 10^{12}\,\mathrm{cm}^{-2}$ (determined by quantum oscillations at $D = 0$).